Effect of Aggregate Size on the Dynamic Interfacial Bond Behaviour between Basalt Fiber Reinforced Polymer Sheets and Concrete

Cheng Yuan[1], Wensu Chen[1]*, Thong M. Pham[1], Li Chen[2], Jian Cui[3], Yanchao Shi[3], Hong Hao[1]*

[1]Centre for Infrastructural Monitoring and Protection, School of Civil and Mechanical Engineering, Curtin University, Australia

[2]School of Civil Engineering, Southeast University, China

[3]Tianjin University and Curtin University Joint Research Center of Structure Monitoring and Protection, School of Civil Engineering, Tianjin University, China

**Corresponding Author*

Abstract

This experimental investigation examines the effect of aggregate size (i.e. 5-10 mm, 10-15 mm, and 15-20 mm) on the dynamic interfacial bond behaviour between BFRP and concrete under various loading speeds (i.e. 8.33E-6, 0.1, 1.0, 3.0, 5.0, and 8.0 m/s). The testing results including the interfacial bond strength and bond-slip responses are evaluated and discussed. For the specimens with the same aggregate size under different loading speeds, the ultimate debonding strain of the BFRP sheets under dynamic loading is greater than that under static loading, and the debonding load and peak shear stress increase significantly with the rising loading speed. For the specimens with different aggregate sizes under the same loading speed, the peak interfacial shear stress slightly reduces with the rising aggregate size. However, the variation of the interfacial shear stress is marginal when the loading speed is over 3 m/s due to the debonding surface shifted from concrete substrate to the concrete-epoxy interface. The proposed bond-slip model by incorporating the effects of aggregate size and strain rate effect matches well with the testing results.

Keywords: Dynamic loading; Strain rate; Aggregate size; Interfacial bond behaviour.

1. Introduction

Concrete structures might experience extreme loads, e.g. earthquakes, collisions, and explosions during its service life. Concrete structure responses to dynamic loadings have been intensively studied [1, 2]. It is well understood that the performance of concrete structure under static and dynamic loads are different, and concrete material is sensitive to strain rate that its compressive and tensile strengths are enhanced with the increase of strain rate [3]. Strain rate sensitivity is due to the time-dependent micro crack growth and the viscoelastic characteristics of the cement paste [4]. Previous studies have also shown that the dynamic increase factor (DIF) of the concrete compressive strength is dependent on both the size and volumetric fraction of coarse aggregate [5]. Hao and Hao [6] established a mesoscale model to investigate the effect of size and volumetric fraction of coarse aggregates on the DIF of the compressive strength. The specimens with a larger portion of coarse aggregates showed a greater DIF compared to the specimens with less contents of aggregates. Tülin et al. [7] carried out an experimental study on the impact of aggregate size on the mechanical properties of concrete and found that increasing the coarse aggregate size leads to a decline in the tensile strength. This is because the area of interfacial transition zone (ITZ) increased and more micro-cracks formed near the aggregate with the increase of aggregate size. Additionally, large aggregates can cause poor interfacial bond between the paste and coarse aggregates [8].

Meanwhile, various strengthening techniques and materials have been used to retrofit existing structures with the increasing load-carrying requirement against possible extreme loadings [9-11]. Fibre-reinforced polymer (FRP), as a popular strengthening composite with high strength to weight ratio and excellent corrosion resistance, has been widely used to strengthen concrete structures [11-13]. Numerous researches on FRP-strengthened concrete structures subjected to different loading conditions have been carried out [14-17]. It was reported that FRP external strengthening was an effective way to enhance structures to resist impact or blast loadings [18-

20]. It was found that the FRP-strengthened concrete structures may experience premature failure in the form of debonding failure resulted from either the flexural cracks or flexural-shear cracks in the concrete [21-23]. To understand the mechanism of the debonding process, single-lap shear tests have been conducted and various models have been proposed [11, 24-26]. However, experimental studies of dynamic interfacial bond behaviour of FRP-concrete interface are very limited in the open literature. Only three experimental studies can be found while the limited results are insufficient to unveil the dynamic interfacial mechanism between FRP and concrete under dynamic loadings [16, 27, 28]. Shi et al. [29] carried out double-lap shear tests and found that the interfacial bond behaviour was strain rate dependent and the ultimate debonding strain and the peak interfacial shear stress increased with strain rate. However, the maximum strain rate in that study was only around 0.1 s^{-1}. Shen et al. [27, 30] also carried out double shear tests and reported that the effective bond length (EBL) decreased with the raise of strain rate. However, the maximum peak strain rate measured in the tests was less than 0.65 s^{-1}. Huo et al. [28] conducted impact tests on FRP-strengthened beams to investigate the interfacial bonding behaviour. The test results showed that the bond capacity was significantly affected by strain rate and the EBL decreased with the rising strain rate. The measured maximum strain rate was about 4.9 s^{-1} in that study.

Meanwhile, very limited studies have concerned about the bond performance between BFRP and concrete with explicitly considering the influences of the aggregate size [31-33]. All the existing studies of the influences of aggregate size on bond behaviour considered static loads only. For example, Pan et al. [33] reported that the shear resistance increased with the rising volumetric fraction of coarse aggregates based on observations in experimental studies on the impact of aggregate content on the bond capacity. Yuan et al. [32] reported that the peak shear stress reduced with the increase of aggregate size as observed in single-lap shear tests. These studies clearly demonstrate that the aggregate size in concrete affects the bond behaviours between FRP and concrete. Researches regarding to the mechanical properties of the dynamic interfacial bond between FRP and concrete with different aggregate sizes have not been reported in literature yet. In this paper, therefore, single-lap shear tests on BFRP-to-concrete joints with various coarse aggregate sizes were conducted under various loading velocities ranging from 8.33E-6 m/s to 8 m/s to study the influences of aggregate size on the dynamic interfacial bond capacity. The strain rate measured in this study reached up to 179.30 s^{-1} under the loading speed of 8 m/s. The dynamic bond-slip model was also proposed based on the testing data to predict the effect of aggregate size on the interfacial bond capacity.

2. Experimental program

2.1 Material properties

Figure 1 illustrates the concrete substrates with different aggregate sizes at which three common sizes were selected for this test program, namely the small 5-10 mm, the medium 10-15 mm, and the large 15-20 mm. The concrete prisms with length of 150 mm, width of 150 mm and height of 300 mm were prepared in this test. The concrete mix design is given in Table 1. The nominal thickness of the unidirectional basalt fibre (BFRP) sheet was 0.12 mm. The tested tensile strength, rupture strain, and elastic modulus of the BFRP/epoxy sheets were 1333 MPa, 1.88%, and 73 GPa, respectively. The adhesive consisting of epoxy resin and hardener at a ratio of 5:1 was used to bond the BFRP sheets. The rupture tensile strength, elastic modulus, and rupture tensile strain of the epoxy resin were 50.5 MPa, 2.8 GPa, and 4.5%, respectively [18].

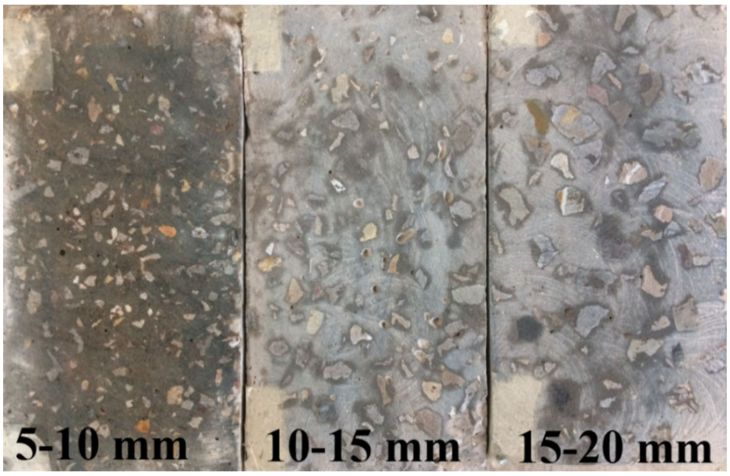

Figure 1. Concrete substrates with different aggregate sizes

Table 1. Concrete mix design and mechanical properties

Group ID	Water/Cement (%)	Sand/Aggregate (%)	Volume percentage of aggregate (%)	Aggregate size (mm)	Compressive strength (MPa)	Tensile strength (MPa)
G1	38	50.4	40	5-10	29.48 30.18 28.74	2.71 2.98 2.86
Mean					29.47 (COV=0.02)	2.85 (COV=0.05)
G2	38	50.4	40	10-15	32.70 33.04 30.09	2.68 2.72 2.62
Mean					31.94 (COV=0.05)	2.67 (COV=0.02)
G3	38	50.4	40	15-20	31.86 34.23 33.09	2.70 2.43 2.51
Mean					33.06 (COV=0.04)	2.55 (COV=0.05)

2.2 Dynamic testing procedure and specimen details

The INSTRON® VHS 160-20 machine was used to carry out dynamic tests. This servo-hydraulic machine is able to provide a controlled speed from 0.1 m/s to 25 m/s, Figure 2 illustrates the test machine and experimental setup. The fast jaw of this machine accelerates until it reaches the designated velocity and then grabs the FRP specimens. The steel jig was carefully designed and firmly fixed to the machine to prevent the concrete blocks from the in-plane and out-of-plane movements. Table 2 gives the specimen details and the results of static and dynamic tests. Fifty-one single-lap specimens were prepared in total. The variables including aggregate size and loading speed are summarized in Table 2.

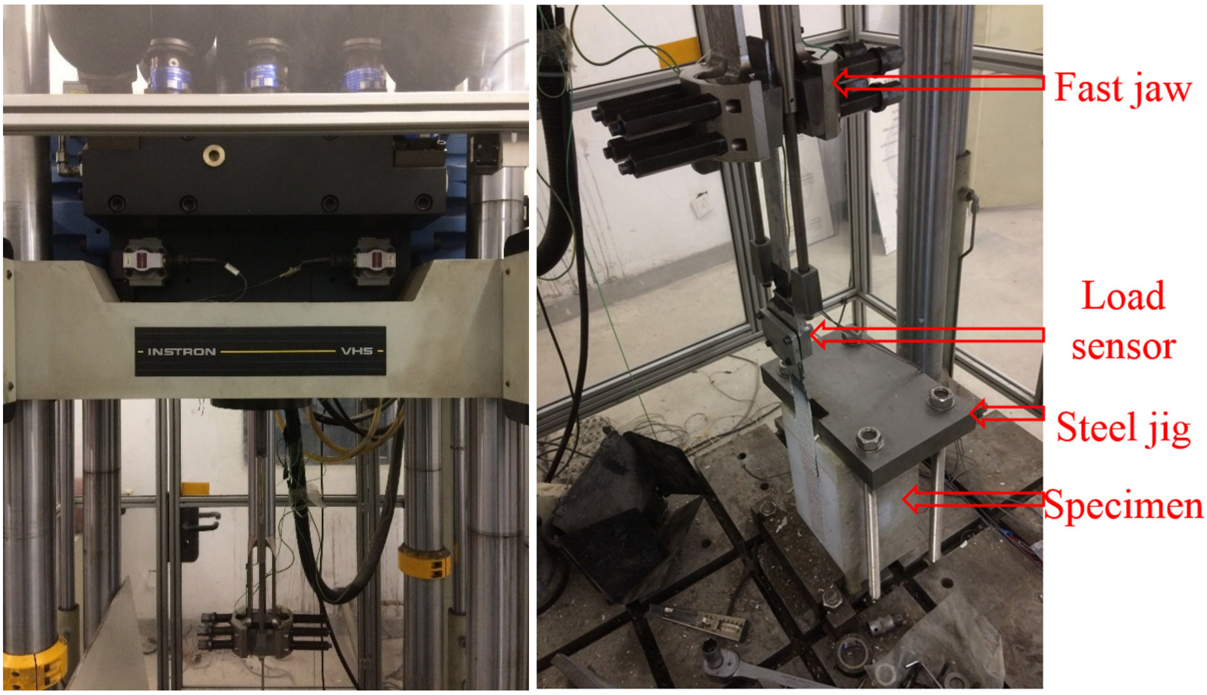

(a) Dynamic single-lap shear test setup

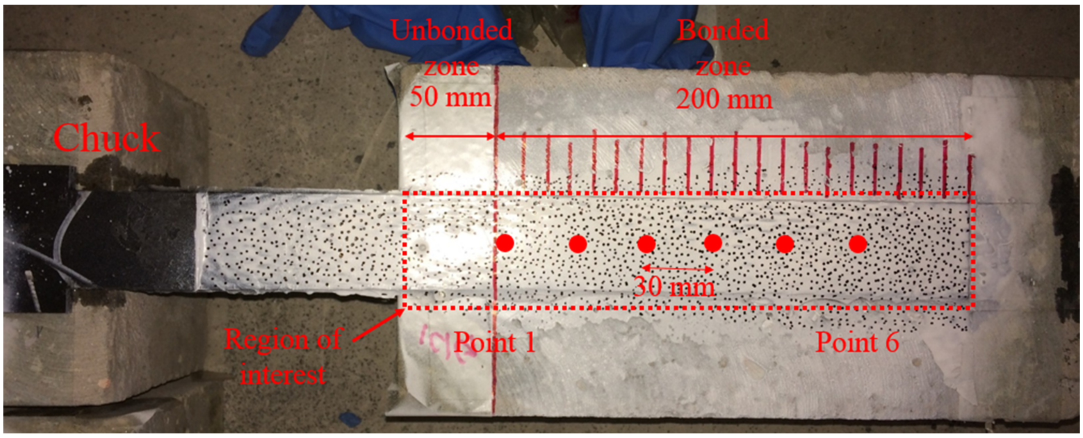

(b) Specimen detail

Figure 2. Testing setup and specimen detail

Table 2. Specimen details and testing results

Specimen ID	Aggregate size (mm)	Loading velocity (m/s)	Strain rate (s^{-1})	P_u (kN)	ε_m (%)	τ_m (MPa)	s_o (mm)	G_f (N/mm)	Failure mode
QS1-1	5-10	8.33E-6	2.50E-05	7.87	1.10	2.20	0.131	1.10	C
QS1-2	5-10	8.33E-6	2.50E-05	6.93	0.99	2.11	0.146	0.86	C
QS2-1	10-15	8.33E-6	2.50E-05	7.34	1.03	2.10	0.128	0.96	C

QS2-2	10-15	8.33E-6	2.50E-05	7.01	0.88	2.07	0.121	0.88	C
QS3-1	15-20	8.33E-6	2.50E-05	7.12	0.98	1.98	0.118	0.90	C
QS3-2	15-20	8.33E-6	2.50E-05	6.87	0.80	1.87	0.116	0.84	C
D1-1	5-10	0.1	4.51	8.07	1.18	3.25	0.130	1.16	C
D1-2	5-10	0.1	4.31	7.88	1.10	2.95	0.141	1.11	C
D1-3	5-10	0.1	4.21	7.67	1.09	2.68	0.135	1.05	C
D2-1	5-10	1.0	25.90	8.34	1.46	4.81	0.132	1.24	C
D2-2	5-10	1.0	33.31	9.86	1.50	4.85	0.140	1.73	C
D2-3	5-10	1.0	29.56	9.72	1.49	4.20	0.128	1.69	C
D3-1	5-10	3.0	65.12	10.51	1.65	5.34	0.124	1.97	C
D3-2	5-10	3.0	57.01	12.32	1.70	6.65	0.130	2.71	C
D3-3	5-10	3.0	60.75	12.08	1.70	6.31	0.121	2.60	C/CE
D4-1	5-10	5.0	110.21	12.23	1.66	7.25	0.108	2.67	C/CE
D4-2	5-10	5.0	104.8	11.78	1.68	7.03	0.118	2.48	C/CE
D4-3	5-10	5.0	110.45	12.21	1.66	6.85	0.120	2.66	C/CE
D5-1	5-10	8.0	173.55	12.01	1.83	9.44	0.107	2.57	C/CE
D5-2	5-10	8.0	155.55	11.89	1.79	9.05	0.098	2.52	C/CE
D5-3	5-10	8.0	150.75	13.50	1.84	9.82	0.112	3.25	C/CE
D6-1	10-15	0.1	5.12	7.53	1.10	3.02	0.122	1.01	C
D6-2	10-15	0.1	4.75	7.41	1.08	2.89	0.132	0.98	C
D6-3	10-15	0.1	5.06	7.27	1.07	2.78	0.135	0.94	C
D7-1	10-15	1.0	31.24	9.40	1.36	3.97	0.110	1.58	C
D7-2	10-15	1.0	29.82	8.87	1.30	4.32	0.131	1.40	C
D7-3	10-15	1.0	30.15	9.07	1.31	4.21	0.113	1.47	C
D8-1	10-15	3.0	73.78	10.23	1.52	5.11	0.138	1.87	C
D8-2	10-15	3.0	68.15	11.06	1.61	5.51	0.119	2.18	C
D8-3	10-15	3.0	59.78	10.77	1.60	4.98	0.115	2.07	C/CE
D9-1	10-15	5.0	121.05	11.78	1.64	7.10	0.114	2.48	C/CE
D9-2	10-15	5.0	117.23	11.17	1.62	7.02	0.103	2.23	C/CE
D9-3	10-15	5.0	110.78	12.21	1.71	6.59	0.101	2.66	C/CE
D10-1	10-15	8.0	144.9	13.02	1.71	8.64	0.104	3.02	C/CE
D10-2	10-15	8.0	150.35	12.19	1.70	8.49	0.110	2.65	C/CE
D10-3	10-15	8.0	155.51	11.19	1.62	8.34	0.098	2.23	C/CE
D11-1	15-20	0.1	5.17	7.19	1.05	2.82	0.118	0.92	C
D11-2	15-20	0.1	4.85	7.03	0.98	2.45	0.121	0.88	C
D11-3	15-20	0.1	5.05	7.34	1.00	2.41	0.115	0.96	C
D12-1	15-20	1.0	28.85	7.93	1.16	3.68	0.110	1.12	C
D12-2	15-20	1.0	30.75	8.13	1.22	4.11	0.120	1.18	C
D12-3	15-20	1.0	34.76	8.48	1.23	4.21	0.103	1.28	C
D13-1	15-20	3.0	78.78	9.38	1.51	5.02	0.138	1.57	C
D13-2	15-20	3.0	75.27	10.06	1.61	5.11	0.125	1.81	C/CE
D13-3	15-20	3.0	69.78	10.40	1.62	5.56	0.102	1.93	C
D14-1	15-20	5.0	120.5	10.78	1.63	7.03	0.114	2.07	C/CE
D14-2	15-20	5.0	121.45	11.68	1.69	7.02	0.112	2.43	C/CE
D14-3	15-20	5.0	118.21	11.09	1.65	6.78	0.104	2.19	C/CE
D15-1	15-20	8.0	179.30	11.93	1.70	8.20	0.118	2.54	C/CE
D15-2	15-20	8.0	155.78	12.89	1.80	8.69	0.102	2.96	C/CE
D15-3	15-20	8.0	158.36	11.73	1.70	8.17	0.101	2.45	C/CE

Note: *C* means debonding in the concrete; *CE* means debonding in the concrete-epoxy interface.

3. Testing results and discussions

Testing results of dynamic single-lap shear tests are valid only when stress equilibrium is achieved. In this study, the stress equilibrium of all the specimens was carefully checked and only those results which satisfy this condition were included. Details of the validation of stress equilibrium are presented in Section 3.2. The accuracy of the DIC technique was verified by matching the readings from strain gauges and those from the DIC technique. The results showed that these methods yielded almost the same measurements as also shown in the previous studies [34, 35].

3.1 Failure mode and debonding load

Table 2 summaries failure modes of the tested specimens. For the specimens experienced low loading speeds (i.e. 8.33E-6 m/s, 0.1 m/s, and 1 m/s), a thin concrete layer beneath the epoxy layer was pulled off, as shown in Figure 3 (a). When the loading speed was over 3 m/s (i.e. 5 m/s and 8 m/s), the debonding pattern changed to a combined failure mode, in which the failure occurred at both the thin concrete layer and the concrete-epoxy interface, as shown in Figure 3 (b). The changed pattern of debonding failure mode indicates that the interfacial shear resistance of FRP-concrete interface was enhanced with strain rate due to the increased tensile strength of the concrete substrate. As shown in Figure 3 (c), it was observed that a certain amount of aggregates was pulled out from the concrete matrix in the specimens with small aggregates (i.e. 5-10 mm) as also observed in a previous study [36]. This might be due to the densely distributed small aggregates which caused relatively higher area ratio of aggregate to mortar on the bond surface of concrete substrates. It was reported that fracture path was prone to spread through the aggregates with the higher ratio of aggregate to mortar and the specimens with higher aggregate content were more sensitive to strain rate [36]. In addition, the pull out of aggregates was not observed in the specimens with large aggregates (i.e. 15-20 mm). It might be because of the higher friction between large aggregates and matrix due to the effective embedment depth [31]. Consequently, the fracture path only spreads through the mortar layer.

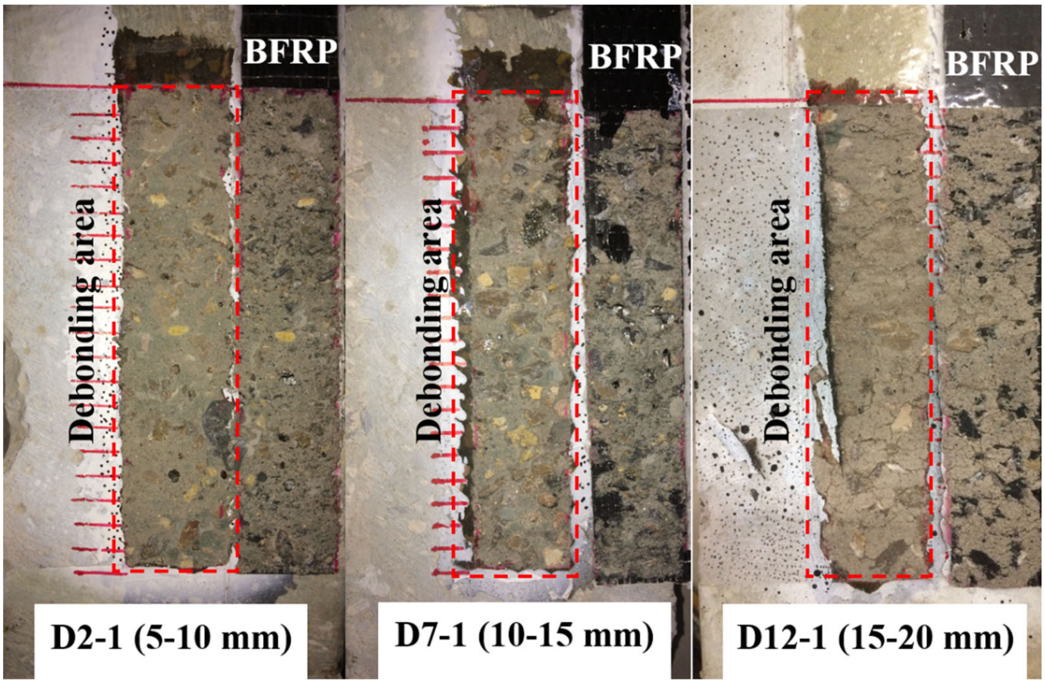

(a) Loading speed of 1 m/s

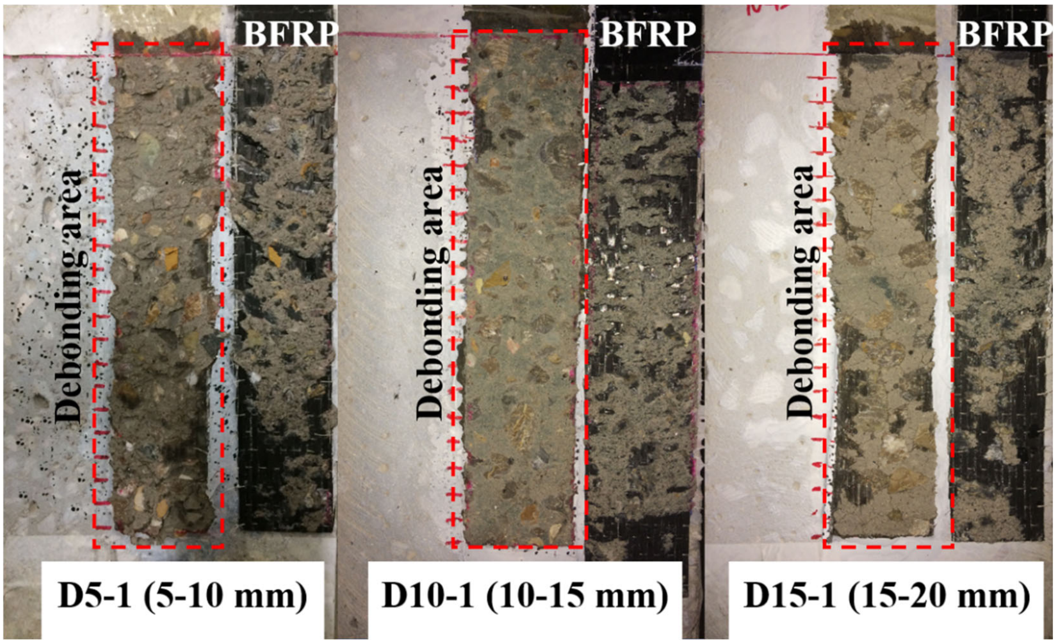

(b) Loading speed of 8 m/s

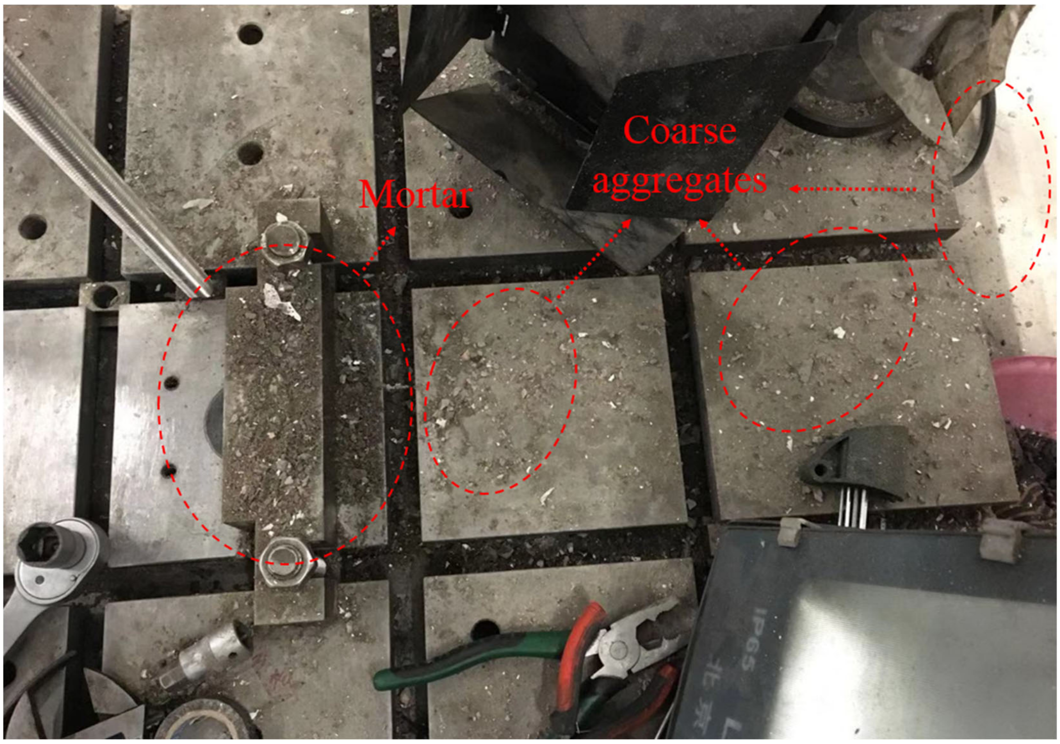

(c) Debris of D3-2 after testing at the loading speed of 3 m/s

Figure 3. Typical failure modes

Figure 4 illustrates the impact of different aggregate sizes on the debonding loads at different loading rates. It was found that the debonding load increased with the loading speed while the increment was marginal when the speed is higher than 3 m/s. Compared to the quasi-static tests, the increment of the debonding load for the specimen D5 (5-10mm), D10 (10-15 mm), and D15 (15-20mm) at the loading speed of 8 m/s was 68%, 69%, and 74%, respectively. The significant increment of the bond strength indicates the enhanced interfacial shear resistance. For the specimens with different aggregate sizes under the same loading speed, the debonding load decreased with the increase of aggregate size, which was caused by the declined tensile strength of concrete with the increasing aggregate size. This phenomenon occurred at almost all the loading speeds. The declined tensile strength is due to the increased micro-cracks caused by stress concentration near the coarse aggregates [7].

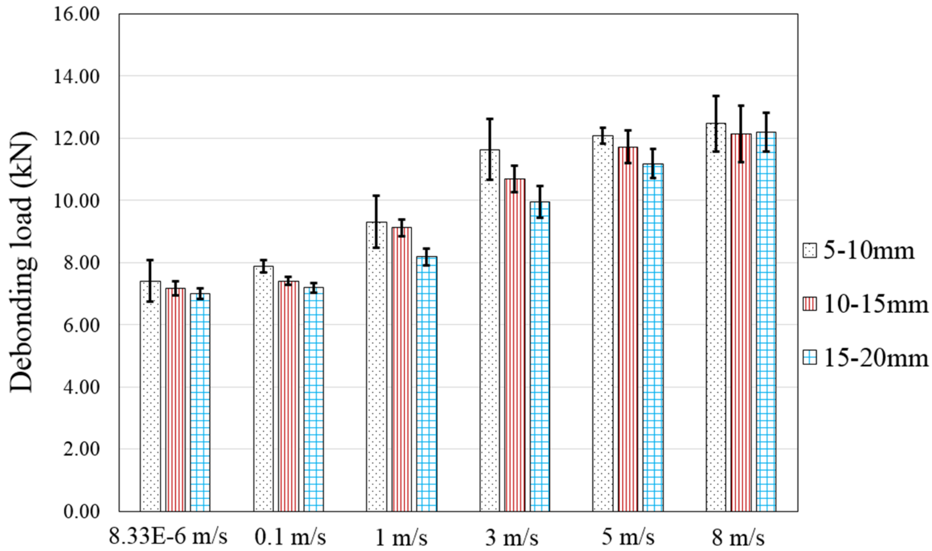

Figure 4. Average debonding load under different loading rates

Figure 5 shows the debris, mostly coarse aggregates, being pulled out from the concrete substrates under dynamic loading speed of 8 m/s. The higher interfacial fracture energy caused by the pull-out of aggregates resulted in a higher debonding load under dynamic loadings. Figure 6 illustrates the effect of the aggregate size on the interlocking action. Small aggregates might result in stronger interlocking action due to their more uniform and dense distribution while large aggregates result in relatively weaker interaction due to the significant spacing between each other. This observation was also found in the effect of various aggregate sizes on the bond behaviour under static loads [32]. Therefore, the stronger interlocking action enhanced the interfacial shear resistance and consequently greater debonding load was resulted in the concrete specimens with small aggregates. Additionally, the interfacial bond strength between BFRP and concrete was proportional to the tensile strength of concrete while the tensile strength would decrease with the rising aggregate size. Therefore, the interfacial bond strength of BFRP-concrete interface declined with the increase of the aggregate size.

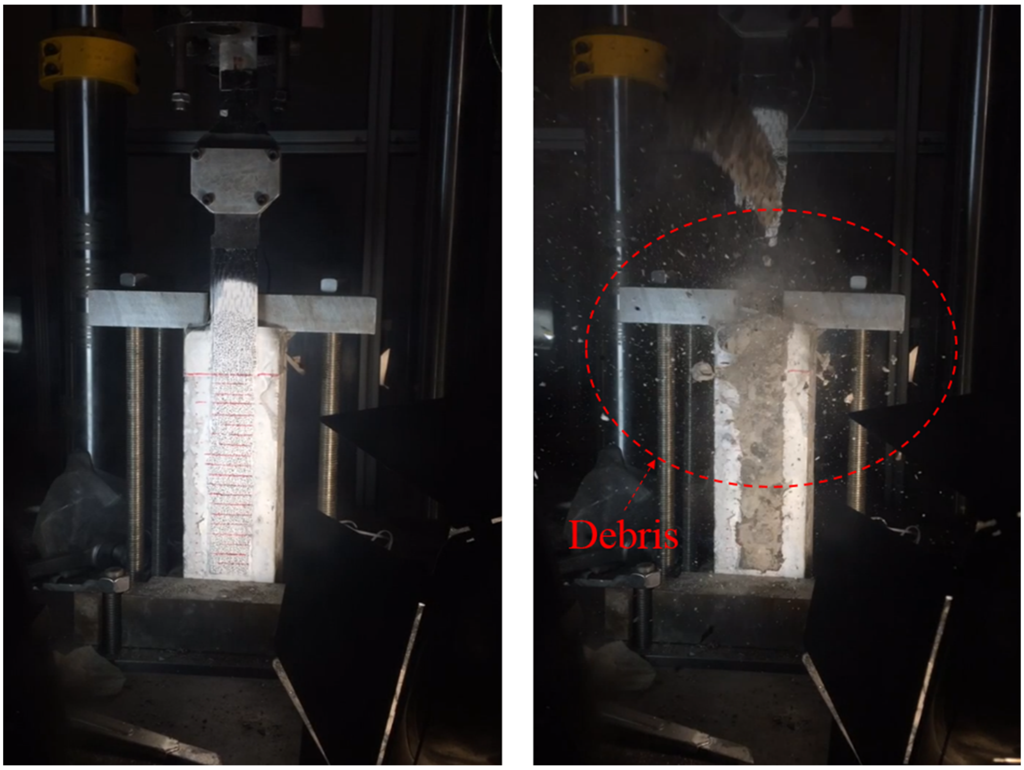

Figure 5. (L) Specimen D15-1 before test; (R) Debris after final debonding

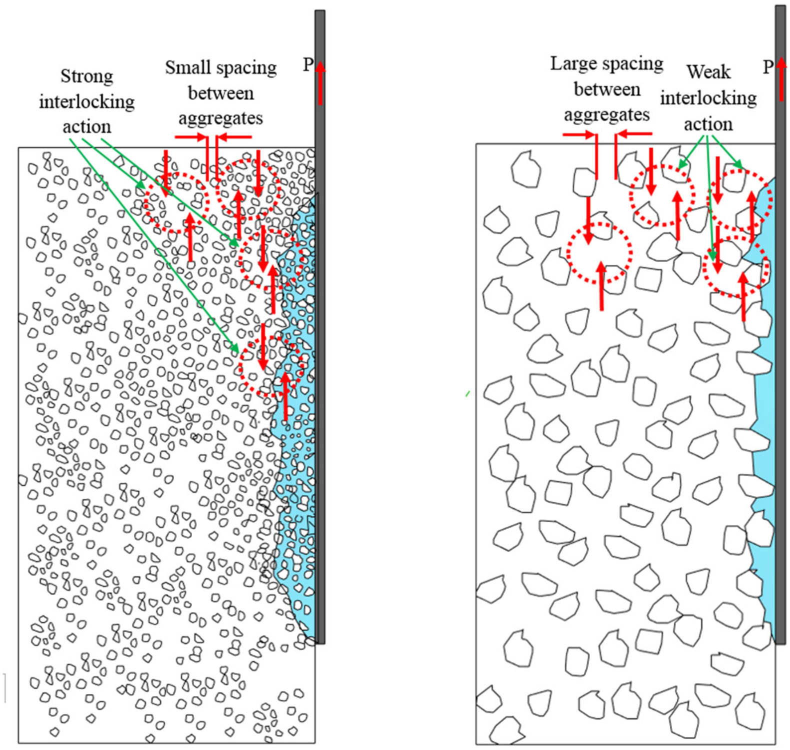

Figure 6. Illustrations of debonding failure process of concrete specimens with small (L) and large (R) aggregates

3.2 Strain rate and dynamic equilibrium

The typical strain contours at various loading stages and loading rates are shown in Figure 7. It is found that all the test specimens show a similar strain contour. The strain contours represented with red, yellow, green and blue colours are obtained from successive digital images. The region with the colours of yellow, red, green and light blue represents the shear stress transfer zone and the dark blue represents the non-stress zone. Meanwhile, the shear stress transfer zone propagated from the loaded end to the free end with the increase of the applied load. It is found that the strain rate and aggregate size have a marginal effect on the patterns of strain distributions since similar strain contours are observed for all the tested specimens. Additionally, the length of the stress transfer zone reaching the initial debonding load can be evaluated by the DIC technique, in which the distance of the shear stress distribution is defined as the effective bond length (EBL) [37, 38].

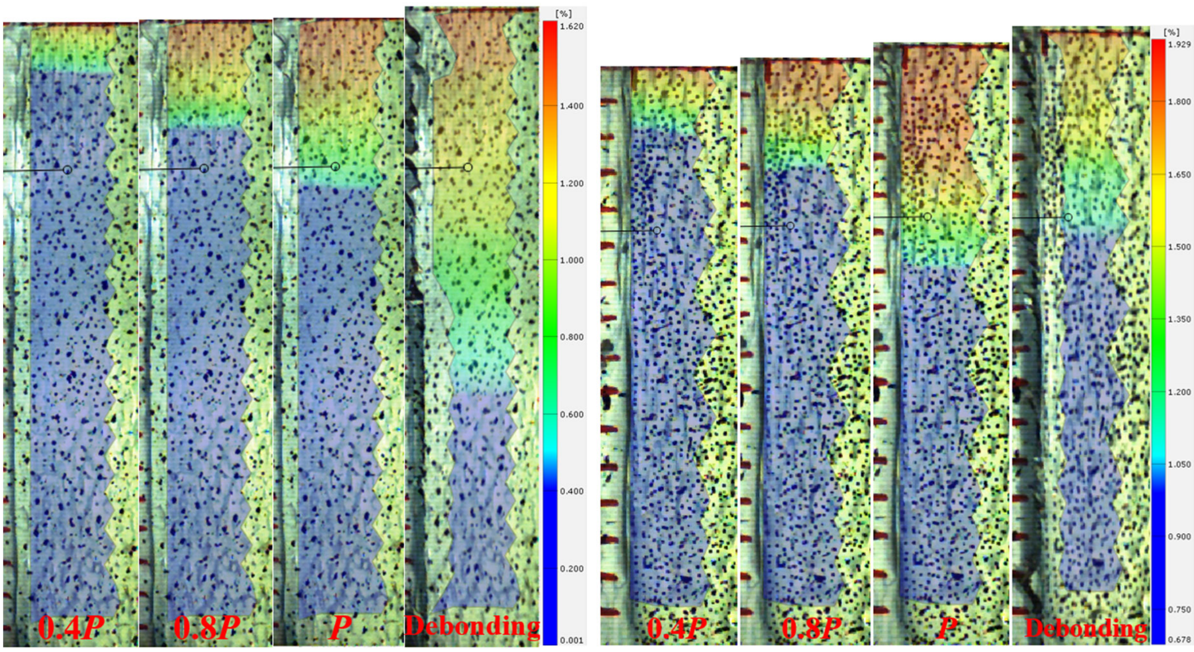

(a) D3-1 (5-10mm; 3 m/s) (b) D5-1 (5-10mm; 8 m/s)

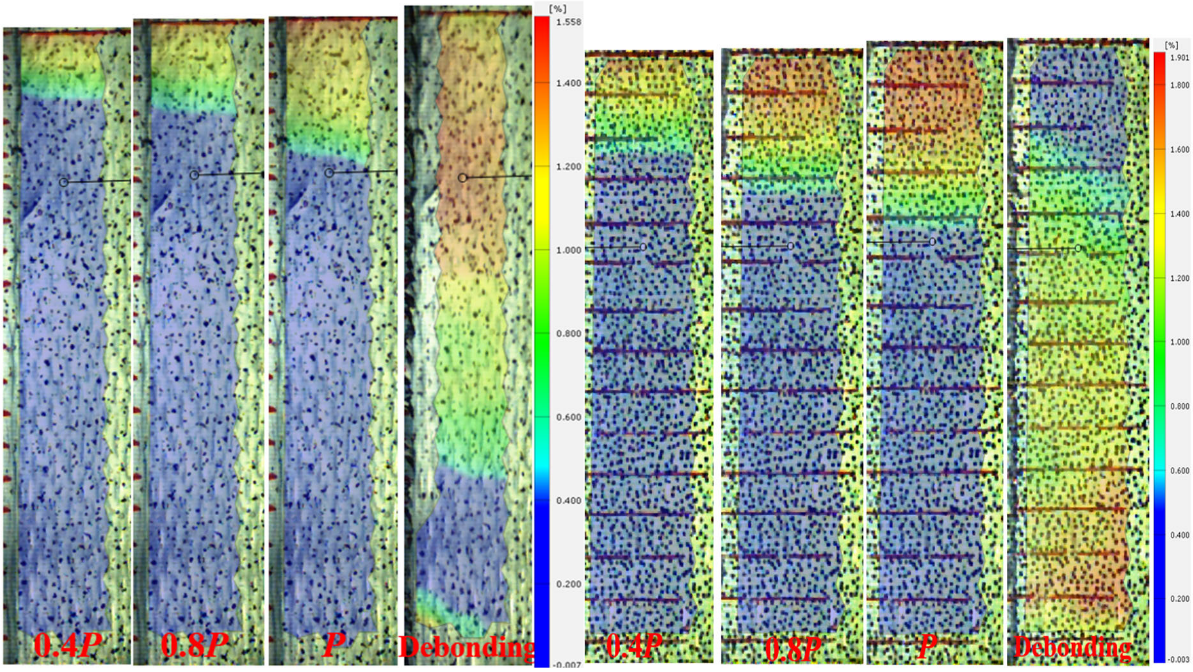

(c) D13-1 (15-20mm; 3 m/s) (d) D15-1 (15-20mm; 8 m/s)

Figure 7. Strain contours of the tested specimens

It was reported that at least three reverberations of stress wave in the specimen were required to achieve the dynamic stress equilibrium [12, 39]. Due to the mixed material properties at the bond interfaces (i.e. concrete, epoxy, and BFRP) of BFRP-to-concrete joint, stress wave velocity cannot be easily obtained using the equation $c = \sqrt{\frac{E}{\rho}}$. To verify the dynamic stress equilibrium, six points (Points 1 to 6) along the centreline of the BFRP sheets are selected and shown in Figure 2 (b). The strain-time histories of Specimens D7-1 (1 m/s) and D10-1 (8 m/s) are plotted in Figure 8. The selected six points (Points 1 to 6) show a similar shape of strain distribution and the strain achieved an approximately plateau, indicating uniform stress distribution. It should be noted that the shape of Point 1 is somewhat different from that at the other points since Point 1 is located at the boundary of the bonded and unbonded regions.

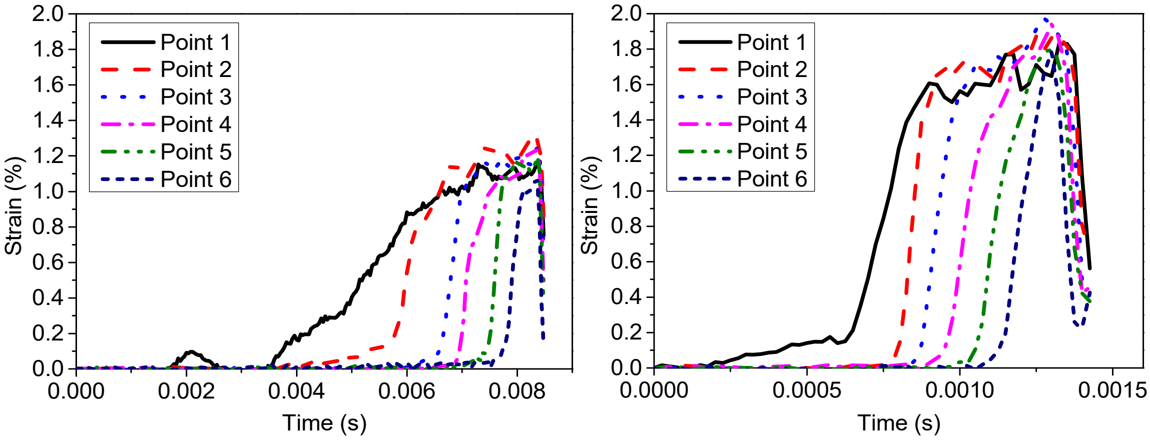

(a) D7-1 (b) D10-1

Figure 8. Strain-time histories

Figure 9 illustrates strain rate distributions along the BFRP sheets at different time instants. The strain rate was obtained by differentiation of the strain time history. Table 2 summarizes the maximum strain rate of all the tested specimens. It is clear that the ultimate strain rate increased with loading rate while varied with loading time and maintained its bell shape to propagate along the BFRP sheets.

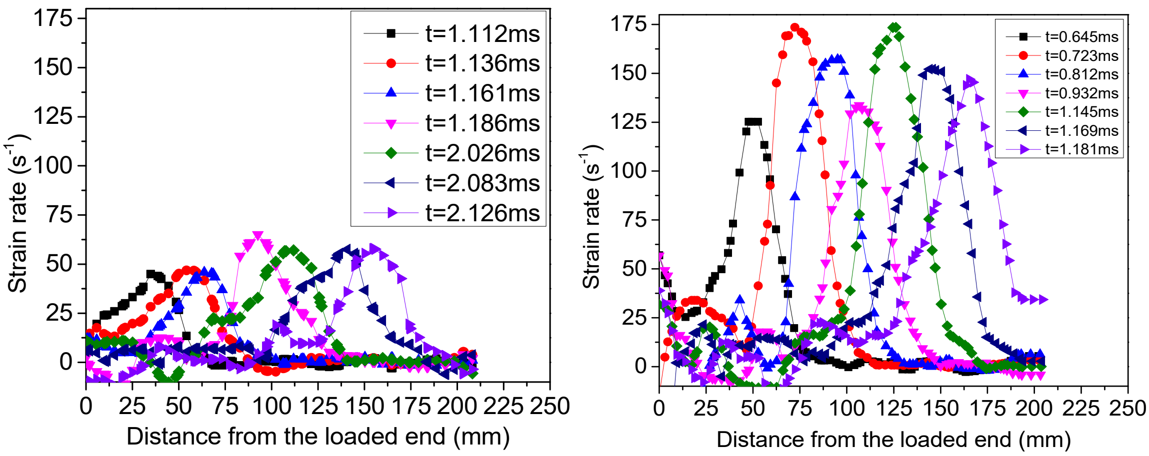

(a) D3-1 (b) D5-1

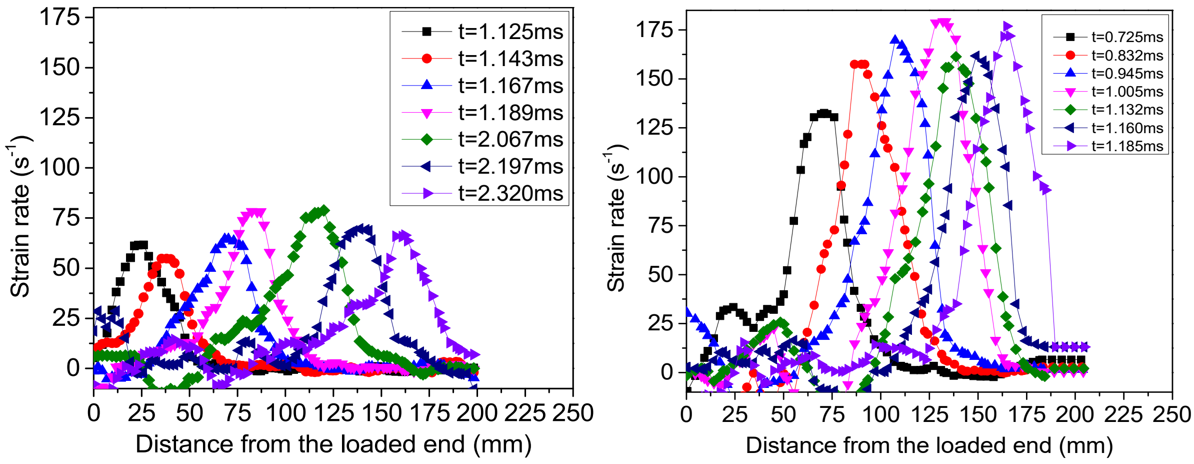

(c) D13-1 (d) D15-1

Figure 9. Strain rate distributions along the bond length

3.3 Strain distribution

Figure 10 illustrates the strain distributions of the BFRP sheets at various loading levels and loading rates. The general trend of the testing results shows that the ultimate debonding strain increased with strain rate and the corresponding test results are summarized in Table 2. The maximum increment of the ultimate debonding strain for Specimen D5 (5-10mm), D10 (10-15mm), and D15 (15-20mm) was 74%, 76%, and 95% at the loading speed of 8 m/s, respectively, when compared to the quasi-static testing results. The increment indicates the enhanced shear resistance between BFRP and concrete. Increasing the size of aggregates resulted in a reduction of the ultimate debonding strain, which is shown in Figure 10 (a, c, and e). This is because of stronger interlocking action for smaller aggregates to resist micro-cracks in the concrete. For the specimens with large aggregates, only the weak layer of mortar was involved in debonding since no pull-out of large aggregates was observed from the tests. Additionally, there was no further increment of the ultimate strain after the initial debonding load P_u and the ultimate strain almost kept its "*S*" shape propagating until final detachment. It is observed that the strain profile along the BFRP sheets under dynamic loading was steeper than that under static loading, indicating that the distance of stress transfer zone decreased with the rising strain rate.

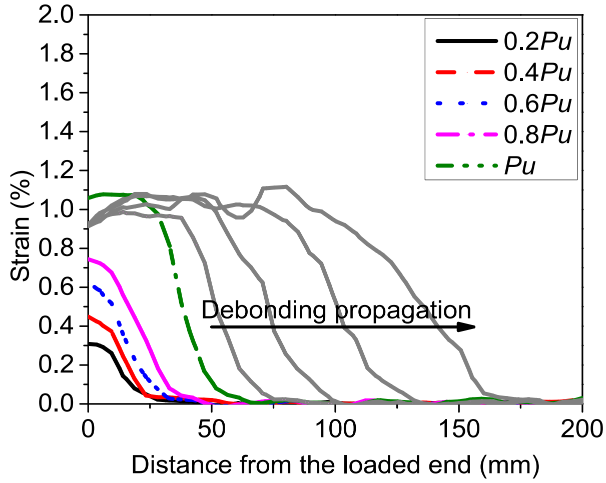

(a) QS1-1 (5-10mm)

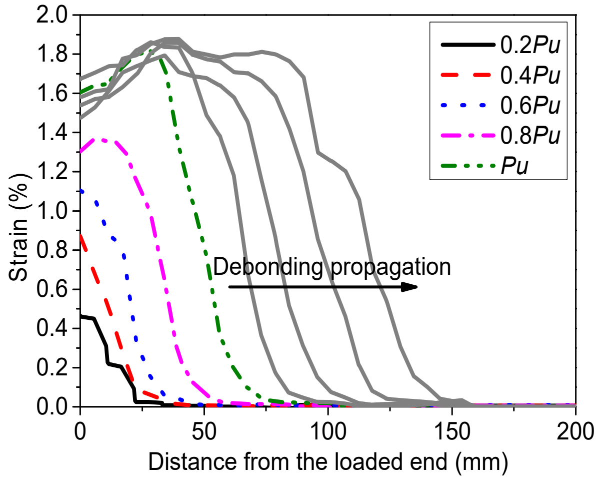

(b) D5-1 (5-10mm)

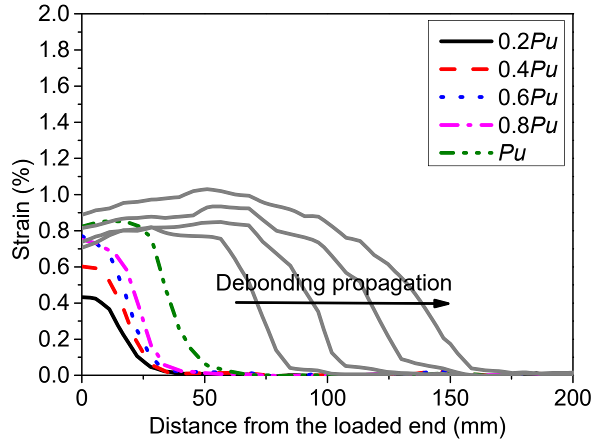

(c) QS2-1 (10-15mm)

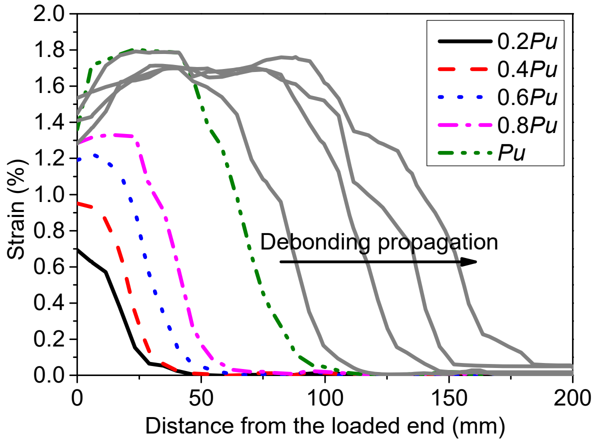

(d) D10-1 (10-15mm)

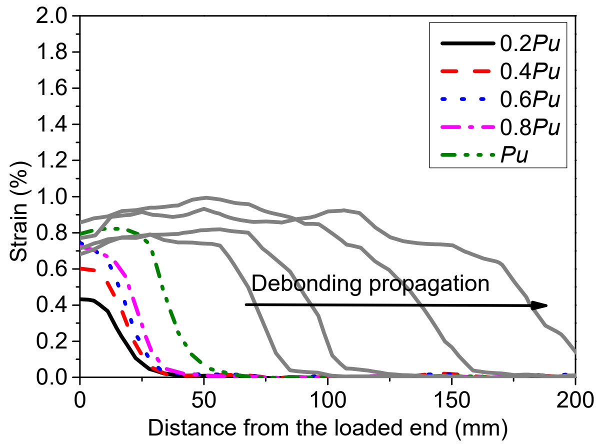

(e) QS3-1 (15-20mm)

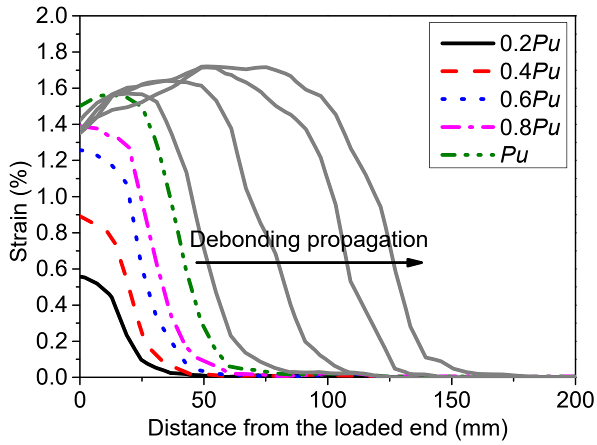

(f) D15-1 (15-20mm)

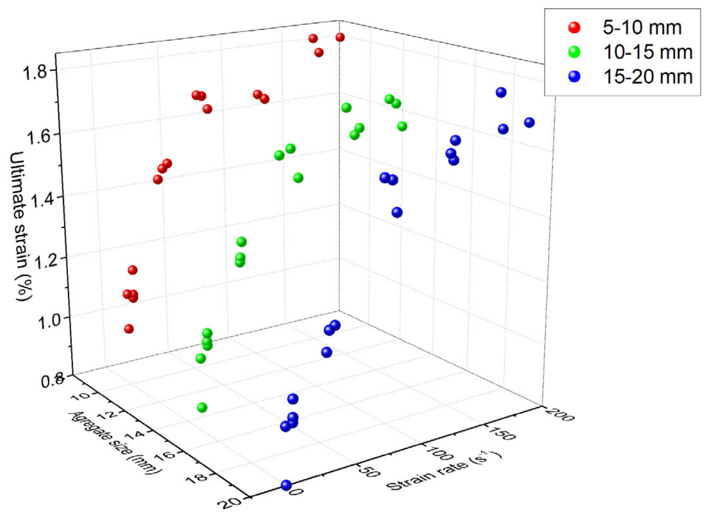

(g) Effect of aggregate size on the ultimate strain at various strain rates

Figure 10. Strain distributions of the tested specimens

3.4 Experimental curve of bond-slip

Figure 11 illustrates the relationship between shear stress and shear slip of the tested specimens. Four loading levels after the initial deboning stage were selected to form a standardized bond-slip response. The distances of 85 mm, 115 mm, 145 mm, and 175 mm shown in the legend represent the range of strain distribution at the four loading stages after reaching an initial debonding load. The stress values at these four loading levels are averaged to obtain the peak shear stress. Because of cracking of concrete, the local bond-slip curve of the BFRP-to-concrete interface shows a nonlinear relationship, i.e. nonlinear ascending and descending branches [40]. It is found that the obtained bond-slip curves from tests are fluctuated, which affects the accuracy of data selection of the peak shear stress and the corresponding slip. Therefore, a widely used nonlinear formula $\tau(s) = \frac{E_f t_f \alpha}{\beta^2}\left(e^{-\frac{s}{\alpha}} - e^{-2\frac{s}{\alpha}}\right)$ for fitting the bond-slip relationship was used to average and smoothen the local bond-slip relationship [24, 25, 41-43]. Similar bond-slip curves can be observed for all the tested specimens. The peak shear stress increased significantly with strain rate for the specimens with the same size of aggregates due to the increased ultimate debonding strain with the strain rate. The maximum increment of the peak shear stress for Specimens D5, D10, and D15 was 77%, 75%, and 74%, respectively, as compared to the corresponding quasi-static testing results. However, the peak shear stress reduced with the increase of aggregate size for the specimens at the same loading rate, as shown in Figure 12 (a). Additionally, the test results show that the interfacial fracture energy G_f, which is the enclosed area under the bond-slip curve, increased with the strain rate while decreased with the rising aggregate size, as shown in Figure 12 (b). However, the variation of interfacial fracture energy was marginal when the loading speed was over 5 m/s because of the shifted debonding surface from concrete layer to the interface of concrete-epoxy.

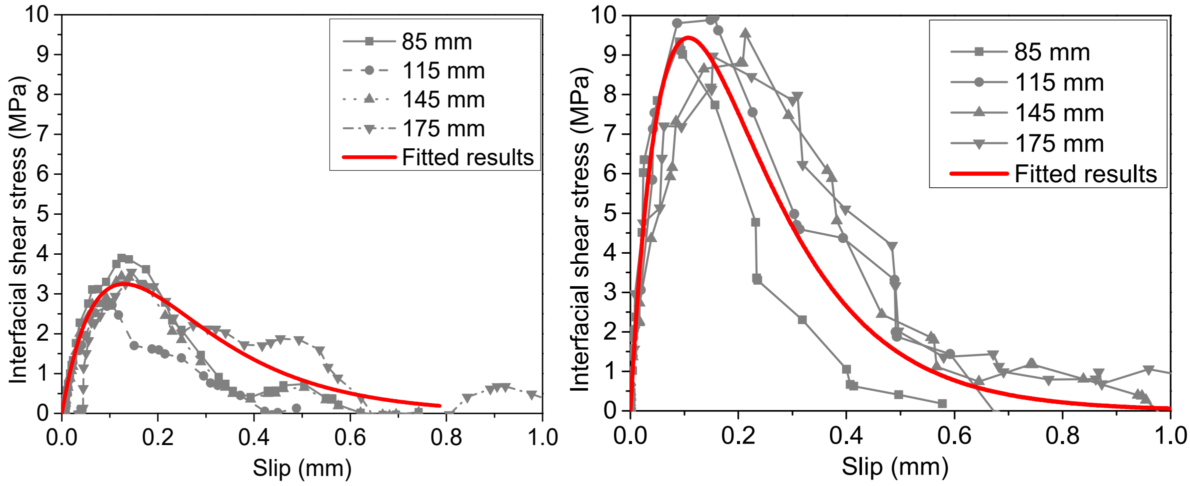

(a) QS1-1 (5-10mm)

(b) D5-1 (5-10mm)

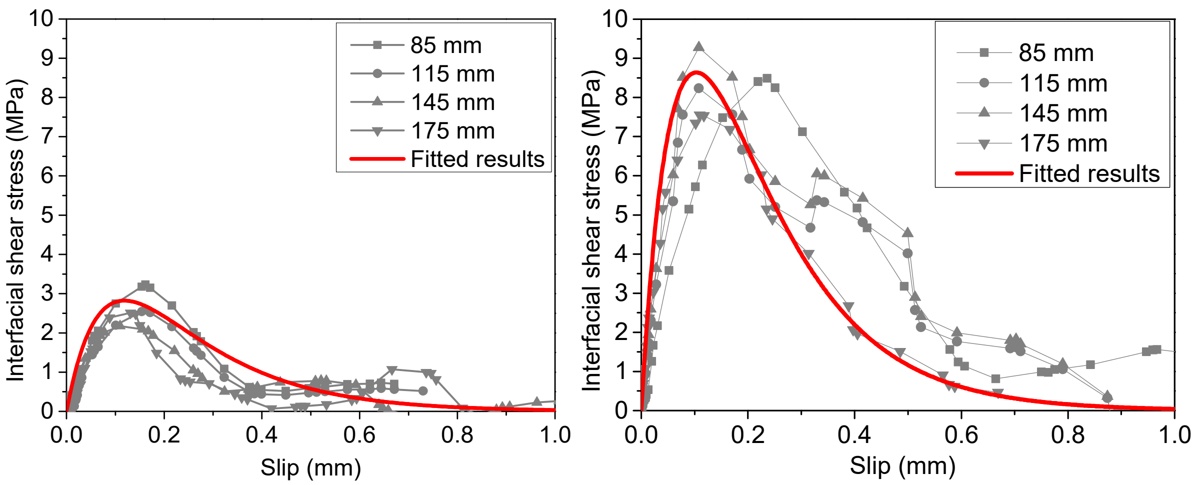

(c) QS2-1 (10-15 mm)

(d) D10-1(10-15 mm)

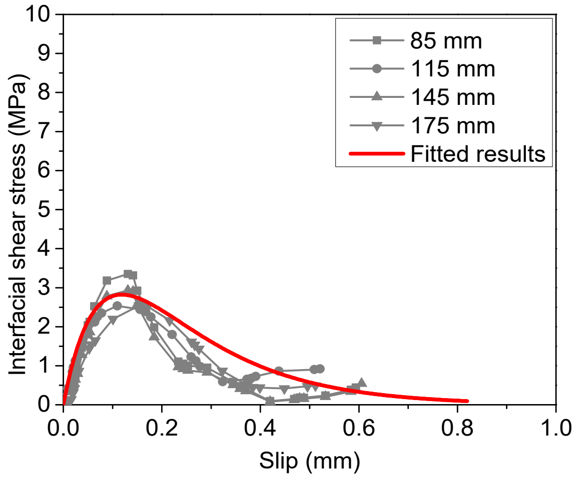

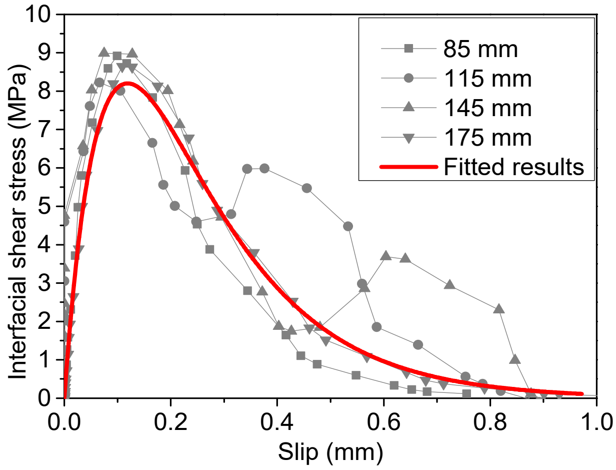

(e) QS3-1 (15-20 mm) (f) D15-1(15-20 mm)

Figure 11. Typical bond-slip curves of the tested specimens at different loading speeds

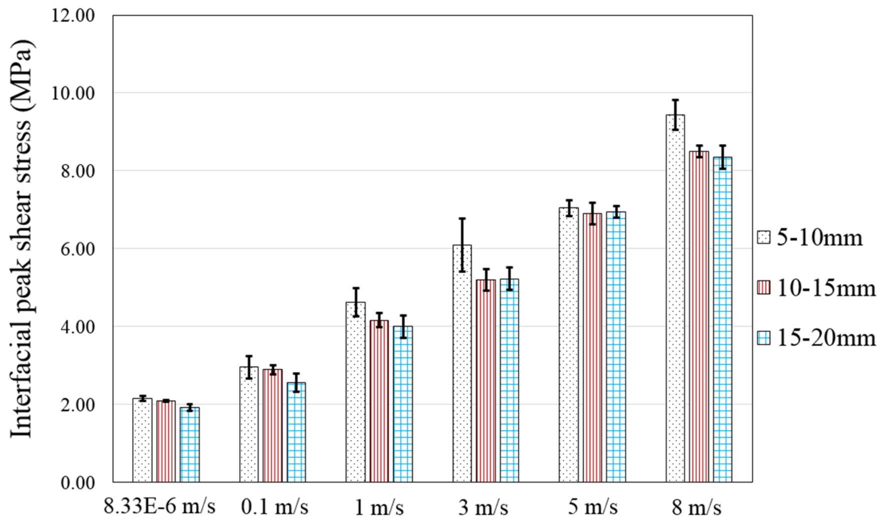

(a) Peak shear stress vs loading rate

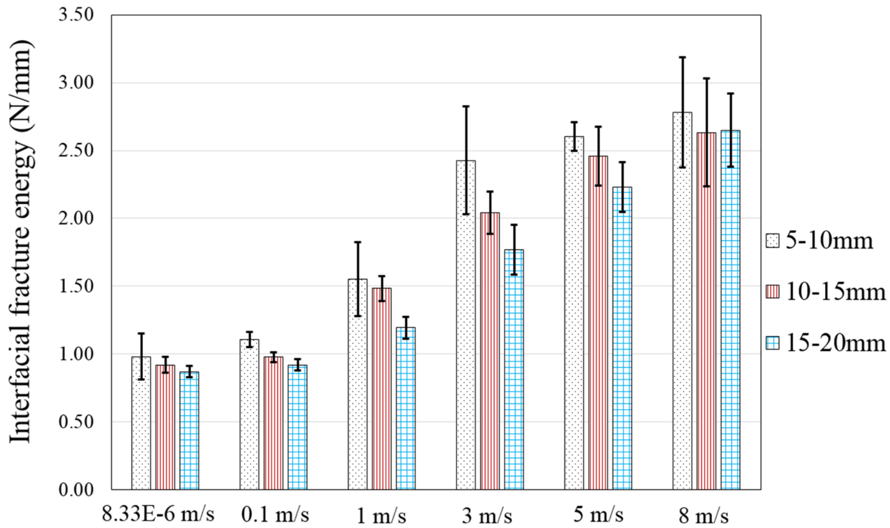

(b) Interfacial fracture energy vs loading rate

Figure 12. Effect of loading rate on the peak shear stress and interfacial fracture energy

4. Analytical investigation and proposed models

4.1 Effect of aggregate size on concrete properties

The general trend of the test results shows that the compressive strength increased while the tensile strength of concrete decreased with the increased aggregate size, as shown in Figure 13. This is because larger aggregates lead to a weak interfacial transition zone (ITZ) as well as the increased micro-cracks near the aggregates as reported in previous studies [7, 44]. Therefore, Equations (1) and (2), proposed by the previous study [45], were adopted to obtain the compressive strength and tensile strength of concrete respectively:

$$f_c = 1.398 f_c^{'} - \frac{7.265 f_c^{'}}{\sqrt{1 + \frac{d_{max}}{0.06263}\left(\frac{h}{d} - 0.07717\right)}} \tag{1}$$

$$f_t = 28.2 (f_c)^{-0.6817} \tag{2}$$

where f_t is the predicted tensile strength of concrete, f_c (MPa) is the predicted compressive strength of concrete, $f_c^{'}$ is the designed compressive strength which is 30 MPa in this study, d_{max} (mm) is the maximum aggregate size, and h and d are the height and diameter of the concrete cylinder, respectively.

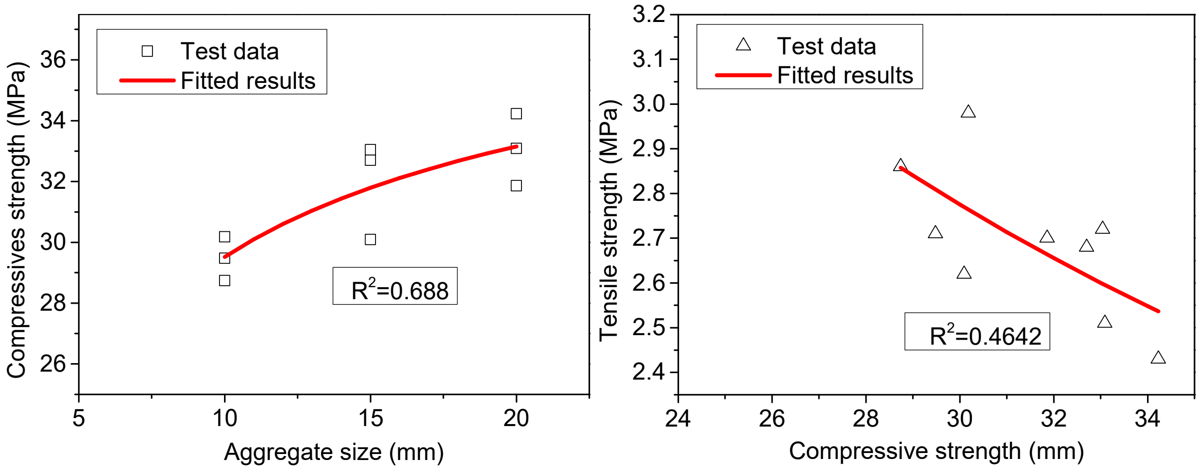

Figure 13. Fitted results of compressive and tensile strength of concrete with different aggregate sizes

4.2 Modelling of interfacial fracture energy

The shear stress and slip response depends on the interfacial fracture energy (G_f). The interfacial fracture energy can be calculated by the enclosed area of bond-slip curves or derived from the debonding load. It is noted that interfacial fracture energy or bond-slip curves were not given in some previous studies but the debonding load was usually provided in most studies as listed in Table 3 and 5. Therefore, for easy comparison with the selected data, the interfacial fracture energy G_f of each specimen was calculated based on the debonding load in this study. A widely accepted and applied formula for the calculation of the interfacial fracture energy can be expressed as follows [24]:

$$G_f = \frac{P_u^2}{2b_f^2 t_f E_f} \tag{3}$$

in which P_u is the debonding load, and E_f, t_f, and b_f are the elastic modulus, thickness, and width of BFRP sheets, respectively.

Table 2 summarizes the interfacial fracture energy of all the tested specimens. The general trend of the test results shows that the interfacial fracture energy decreased with the rising aggregate size under both static and dynamic loadings, but the reduction became marginal for the loading velocity over 3 m/s. The threshold of 3 m/s is resulted from changing the debonding failure mode i.e. fracture surface shifted from concrete layer to the concrete-epoxy interface. For the specimens with the same aggregate size under different loading rates, the interfacial fracture energy increased with strain rate, as shown in Figure 14 (a). Due to the observed fracture of the adhesive layer over the loading speed of 3 m/s, the model of interfacial fracture energy should take into account the contribution of the adhesive. Based on the study of Wang and Wu [46], the tensile strain energy of adhesive $\frac{f_a^2}{2E_a}$, which is the enclosed area of the uniaxial tensile stress-strain curves reflecting the strength and ductility of the adhesive, was incorporated into the proposed model. To expand the application of the proposed models, a total of 32 specimens collected from the previous studies were used to conduct the regression analysis [28, 30, 47-49]. The details of the collected 32 tests are summarized in Table 3. Furthermore, the tensile strength of concrete in the form of $\sqrt{f_t}$, the width ratio of FRP to concrete in the form of β_w^2 are the factors determining the interfacial fracture energy. The static and dynamic interfacial fracture energies can be predicted by the following equations:

$$G_{f,s} = 0.55\beta_w^2\left(\frac{f_a^2}{2E_a}\right)^{0.42}\sqrt{f_t} \tag{4}$$

$$\frac{G_{f,d}}{G_{f,s}} = 1 + 1.096\times10^{-8}\left(\log\left(\frac{\dot{\varepsilon}_d}{\dot{\varepsilon}_s}\right)\right)^{9.09} \quad \text{when } 2.5\times10^{-5} \le \dot{\varepsilon} \le 179.30 \tag{5}$$

$$\beta_w = \sqrt{\frac{2.25 - b_f/b_c}{1.25 + b_f/b_c}} \tag{6}$$

where f_a is the tensile strength of adhesive, E_a is the elastic modulus of adhesive, f_t is the tensile strength of concrete, $G_{f,s}$ is the static interfacial fracture energy, $G_{f,d}$ is the dynamic interfacial fracture energy, β_W is the width ratio of FRP to concrete, b_f is the width of BFRP, and b_c is the width of the concrete substrate. Figure 14 (b) compares the predicted results with the experimental results. The predicted results almost coincide with the test data as the mean value of the ratio of the predicted to experimental results is 0.95 and the corresponding coefficient of variation (COV) is 0.12.

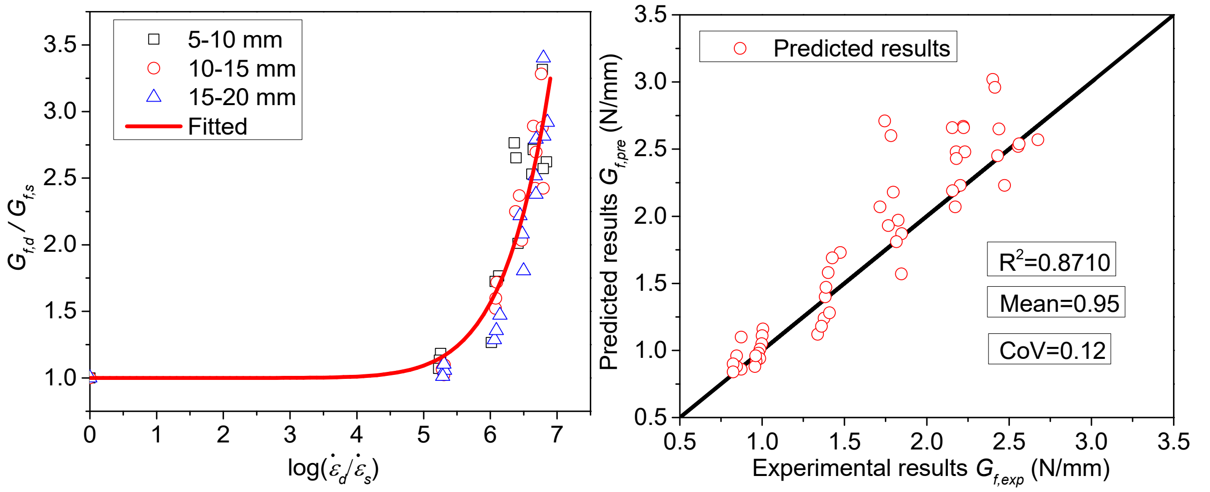

(a) (b)

Figure 14. (a) Interfacial fracture energy ratio vs. strain rate; (b) Comparison between experimental and predicted interfacial fracture energy

Table 3. Data collected from previous studies for tensile strain energy of adhesive

Reference	Specimen ID	Test method	Adhesive			FRP			Concrete	$P_{u,exp}$ (kN)
			f_a (MPa)	E_a (GPa)	$f_a^2/2E_a$ (N/mm^2)	E_f (GPa)	t_f (mm)	b_f (mm)	f_t (MPa)	
Present study	QS1-1	Single shear	50.50	2.8	0.455	73	0.240	40	2.85	7.87
	QS1-2		50.50	2.8	0.455	73	0.240	40	2.85	6.93
	QS2-1		50.50	2.8	0.455	73	0.240	40	2.67	7.34
	QS2-2		50.50	2.8	0.455	73	0.240	40	2.67	7.01
	QS3-1		50.50	2.8	0.455	73	0.240	40	2.54	7.12
	QS3-2		50.50	2.8	0.455	73	0.240	40	2.54	6.87
Shen et al. [30]	L200-1	Double shear	45.80	2.6	0.403	105	0.121	50	2.62	11.40
	L200-2		45.80	2.6	0.403	105	0.121	50	2.62	10.80
	L200-3		45.80	2.6	0.403	105	0.121	50	2.62	13.60
Huo et al. [28]	C50-1-1	Beam	65.00	3.2	0.660	236	0.169	50	2.89	13.60
	C50-1-2		65.00	3.2	0.660	236	0.169	50	2.89	11.50
	C50-2-1		65.00	3.2	0.660	236	0.338	50	2.89	18.00
	C50-2-2		65.00	3.2	0.660	236	0.338	50	2.89	14.20
	C80-2-1		65.00	3.2	0.660	236	0.338	80	2.89	17.50
	C80-2-2		65.00	3.2	0.660	236	0.338	80	2.89	18.40
Toutanji et al. [47]	A-1	Single shear	23.60	4.1	0.068	110	0.495	50	2.73	7.56
	A-2		23.60	4.1	0.068	110	0.660	50	2.73	9.29
	A-3		23.60	4.1	0.068	110	0.825	50	2.73	11.64
	B-4		23.60	4.1	0.068	110	0.990	50	2.73	12.86
	B-1		23.60	4.1	0.068	110	0.495	50	2.73	12.55

	B-2		23.60	4.1	0.068	110	0.660	50	2.73	14.25
	B-3		23.60	4.1	0.068	110	0.825	50	2.73	17.72
	B-4		23.60	4.1	0.068	110	0.990	50	2.73	18.86
	C-1		23.60	4.1	0.068	110	0.495	50	2.73	13.24
	C-2		23.60	4.1	0.068	110	0.660	50	2.73	15.17
	C-3		23.60	4.1	0.068	110	0.825	50	2.73	18.86
	C-4		23.60	4.1	0.068	110	0.990	50	2.73	19.03
Yun et al. [48]	M-EB	Double shear	54.00	3.0	0.289	257	0.660	50	3.03	26.30
Yun and Wu [49]	N30-0-1	Single shear	45.00	3.5	0.289	235	0.167	50	2.81	23.70
	N30-0-2		45.00	3.5	0.289	235	0.167	50	2.81	24.40
	N45-0-1		45.00	3.5	0.289	235	0.167	50	3.22	27.70
	N45-0-2		45.00	3.5	0.289	235	0.167	50	3.22	27.40

Note: $f_t = 0.53\sqrt{f_c}$ (MPa) [50].

4.3 Modelling of dynamic bond-slip

Popovics's equation [51] was used to describe the bond-slip relationship in this study as this equation has been widely used by numerous studies to predict the bond-slip response [52, 53]. Two branches of the bond-slip curves including the ascending and descending obtained by the Popovics's equation match well with the experimental shear stress and slip curves, as shown in Figure 15. The formula of the Popovics's equation is shown in the following equation:

$$\tau(s) = \tau_m \left(\frac{s}{s_o} \frac{n}{(n-1) + (s/s_o)^n} \right) \tag{7}$$

in which τ_m is the peak shear stress, s_o is the maximum shear slip at the peak shear stress, and n is the coefficient determining the shape of bond-slip curves. The dynamic bond-slip curve can be obtained by replacing the static peak shear stress $\tau_{m,s}$ with the dynamic one $\tau_{m,d}$. The regression coefficient n and the corresponding least square R^2 are summarized in Table 4. The predicted results of Popovics's equation are consistent with the testing results with the highest correlation coefficient given in Table 4.

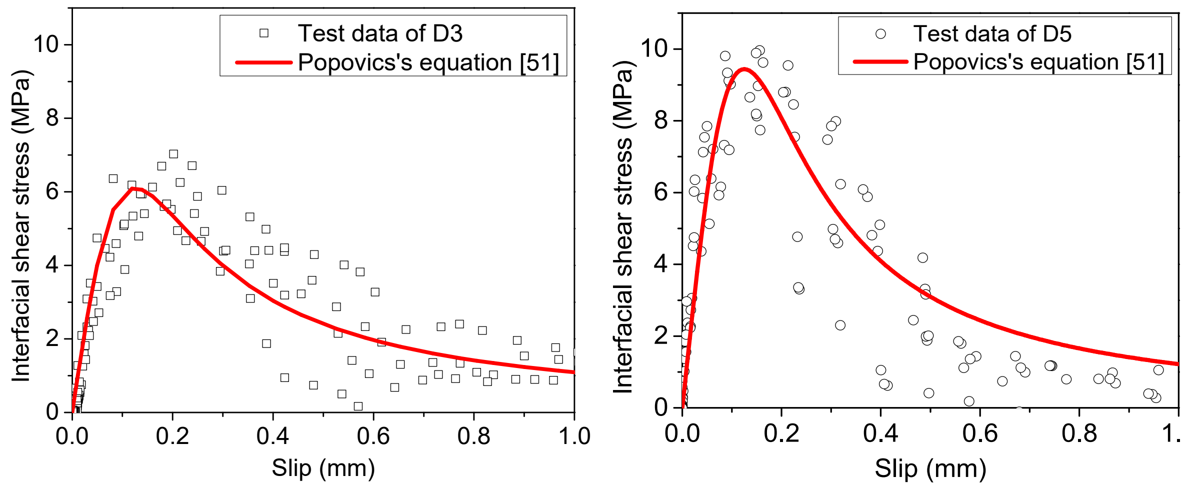

(a) D3 (b) D5

Figure 15. Fitted bond-slip curves

Table 4. Experimental results and regression coefficients

Specimen ID	Loading speed (m/s)	Peak shear stress τ_m (MPa)	Slip s_o (mm)	Coefficient n	Correlation coefficient R^2
QS1	8.33E-6	2.16	0.125	2.221	0.8998
QS2	8.33E-6	2.09	0.117	2.109	0.9056
QS3	8.33E-6	1.93	0.114	2.021	0.8789
D1	0.1	2.96	0.125	2.264	0.8878
D2	1	4.62	0.125	2.444	0.8058
D3	3	6.10	0.125	2.512	0.8830
D4	5	7.04	0.125	2.507	0.8574
D5	8	9.44	0.125	3.602	0.8075
D6	0.1	2.90	0.117	2.098	0.8869
D7	1	4.17	0.117	2.724	0.8989
D8	3	5.20	0.117	3.278	0.8787
D9	5	6.90	0.117	3.307	0.8966
D10	8	8.49	0.117	2.687	0.8983
D11	0.1	2.56	0.114	2.002	0.8515
D12	1	4.00	0.114	2.708	0.7519
D13	3	5.23	0.114	3.167	0.8567
D14	5	6.94	0.114	3.385	0.8073
D15	8	8.35	0.114	2.275	0.8736
Mean			0.118	2.628	
COV			0.040	0.200	

The coefficient n slightly increases with the strain rate while the aggregate size has a rather marginal effect on the coefficient n. Given the scattered data, it is difficult to correlate the coefficient n with both strain rate and aggregate size due to the low correlation coefficient. As a result, the coefficient n was set as a constant of 2.628 in the proposed analytical model and the mean value and the corresponding coefficient of variation are summarized in Table 4. Based on the test results of the present study, the peak shear stress increased but the maximum slip s_o decreased with the increasing strain rate, as shown in Figure 16. However, the adopted maximum slip s_o was set as a constant of 0.118 mm which was the average of all the specimens due to the scattered data.

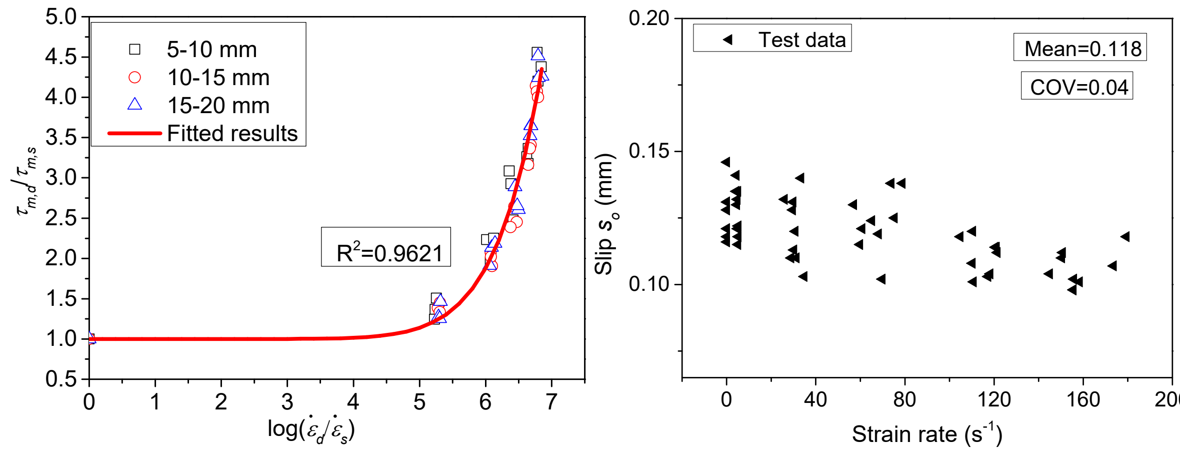

(a) Peak shear stress vs Strain rate (b) Slip vs strain rate

Figure 16. Relationship between strain rate with the peak shear stress and slip

According to the previous peak shear stress models, the tensile strength of concrete (f_t) and the width ratio of FRP-to-concrete (β_w) are the factors determining the peak interfacial shear stress under static loadings [54, 55]. To expand the application of the proposed models, test results of 38 FRP-to-concrete joints were collected from the previous studies as summarized in Table 5 [28, 30, 56-59]. Equations (8) and (9) can be used to obtain the dynamic peak shear stress:

$$\tau_{m,s} = 0.056\beta_w f_t^4 \tag{8}$$

$$\frac{\tau_{m,d}}{\tau_{m,s}} = 1 + 1.216 \times 10^{-8} \left(\log\left(\frac{\dot{\varepsilon}_d}{\dot{\varepsilon}_s} \right) \right)^{10.1} \quad \text{when } 2.5 \times 10^{-5} \le \dot{\varepsilon} \le 179.30 \tag{9}$$

where f_t is the tensile strength of concrete, β_W is the width ratio of FRP-to-concrete, $\tau_{m,s}$ is the peak interfacial shear stress subjected to static loads, and $\tau_{m,d}$ is the dynamic peak interfacial shear stress.

Table 5. Data collection from previous studies for peak shear stress

Reference	Specimen ID	FRP			Concrete			τ_m (MPa)	S_o (mm)
		n	b_f (mm)	t_f (mm)	b_c (mm)	f_c (MPa)	f_t (MPa)		
Shen et al. [30]	L200-D0-1	2	50	0.121	100	32.8	3.04	2.95	0.1090
	L200-D0-2	2	50	0.121	100	32.8	3.04	3.59	0.1090
Huo et al. [28]	C50-1-S-1	1	50	0.165	100	28.0	2.80	4.05	0.0980
	C50-1-S-2	1	50	0.169	100	28.0	2.80	3.50	0.0920
	C50-2-S-1	2	50	0.169	100	28.0	2.80	3.28	0.0680
	C50-2-S-2	2	50	0.169	100	28.0	2.80	4.25	0.0780
	C80-2-S-1	2	80	0.169	100	28.0	2.80	4.74	0.0870
	C80-2-S-2	2	80	0.169	100	28.0	2.80	3.47	0.0740
Bizindavyi and Neale [57]	BN6	1	25.4	1.000	150	34.5	3.11	2.14	-
	BN20	2	25.4	2.000	150	34.5	3.11	2.40	-
	BN25	1	25.4	0.330	150	34.5	3.11	2.10	-
	BN32	2	25.4	0.660	150	34.5	3.11	1.80	-
Subramaniam et al. [56]	W-1	1	46	0.167	125	39.0	3.31	6.83	0.0412
	W-2	1	46	0.167	125	39.0	3.31	6.27	0.0319
	W-3	1	46	0.167	125	39.0	3.31	6.70	0.0297
	W-4	1	38	0.167	125	39.0	3.31	6.66	0.0361
	W-5	1	38	0.167	125	39.0	3.31	8.74	0.0283
	W-6	1	25	0.167	125	39.0	3.31	6.66	0.0286
	W-7	1	25	0.167	125	39.0	3.31	6.65	0.0263
	W-8	1	25	0.167	125	39.0	3.31	7.36	0.0333
	W-9	1	19	0.167	125	39.0	3.31	6.72	0.0331
	W-10	1	19	0.167	125	39.0	3.31	6.51	0.0282
Carloni et al. [58]	DS-S1	1	25	0.167	125	35.0	3.14	6.78	0.037
	DS-S2	1	25	0.167	125	35.0	3.14	6.31	0.040
	DS-S3	1	25	0.167	125	35.0	3.14	6.43	0.043
	DS-F4	1	25	0.167	125	35.0	3.14	6.46	0.035
Pellegrino et al. [59]	S1C1a	1	50	0.165	100	63.0	4.21	15.40	0.032
	S1C5c	1	50	0.165	100	58.0	4.04	15.50	0.036
	S1C5d	1	50	0.165	100	58.0	4.04	6.00	0.034
	S2C1a	2	50	0.165	100	63.0	4.21	17.80	0.027
	S2C1b	2	50	0.165	100	58.0	4.04	9.50	0.022
	S2C1c	2	50	0.165	100	58.0	4.04	18.90	0.031
	S3C1a	3	50	0.165	100	63.0	4.21	9.20	0.025
	S3C1b	3	50	0.165	100	58.0	4.04	10.10	0.022
	S3C1c	3	50	0.165	100	58.0	4.04	10.90	0.024
	S3C5a	3	50	0.165	100	63.0	4.21	23.70	0.019
	S3C5b	3	50	0.165	100	58.0	4.04	11.30	0.027
	S3C5c	3	50	0.165	100	58.0	4.04	22.90	0.030

Note: $f_t = 0.53\sqrt{f_c}$ (MPa) [50]; “-“ means unavailable data.

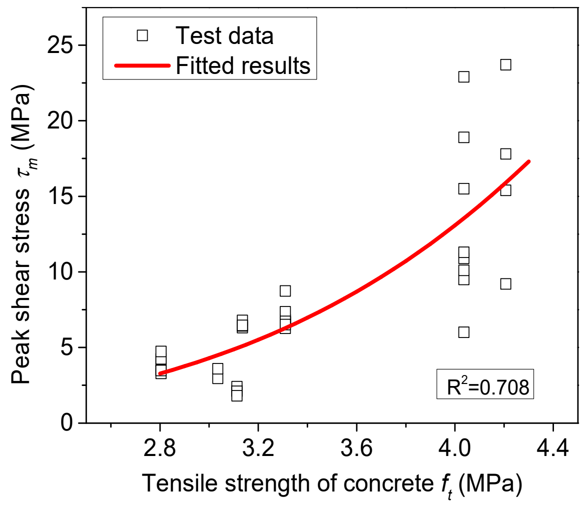

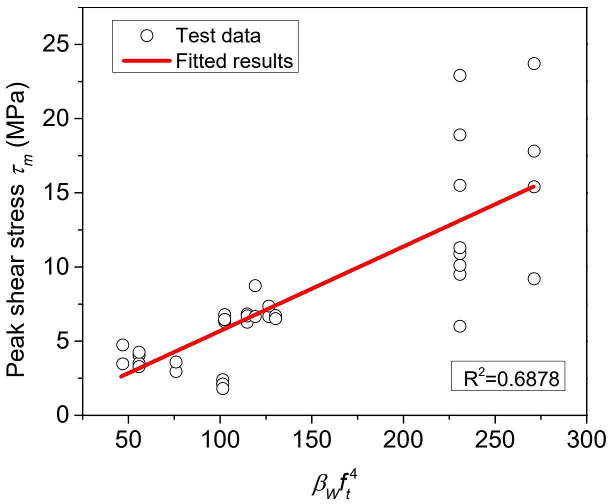

(a) (b)

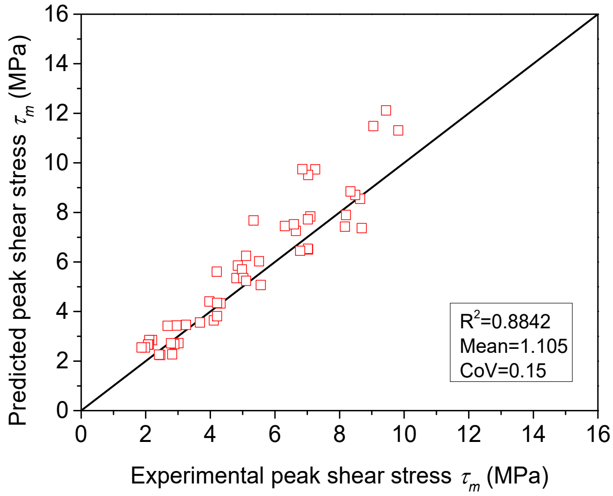

(c)

Figure 17. (a) Peak shear stress vs. tensile strength of concrete; (b) Peak shear stress τ_m vs. $\beta_w f_t^4$, (c) Comparison between experimental and predicted peak shear stress

4.4 Validation of the proposed analytical model

Figure 18 illustrates the predicted shear stress and slip curves by using the Popovics's equation [51]. Equations (8) and (9) are used to obtain the peak shear stress. As shown in Figure 17 (c), the predicted results match well with the experimental results with a mean ratio of 1.105 and a coefficient of variation (COV) of 0.15. The predicted bond-slip response are consistent with the experimental results, namely the peak shear stress increases with strain rate while decreases with the rising aggregate size.

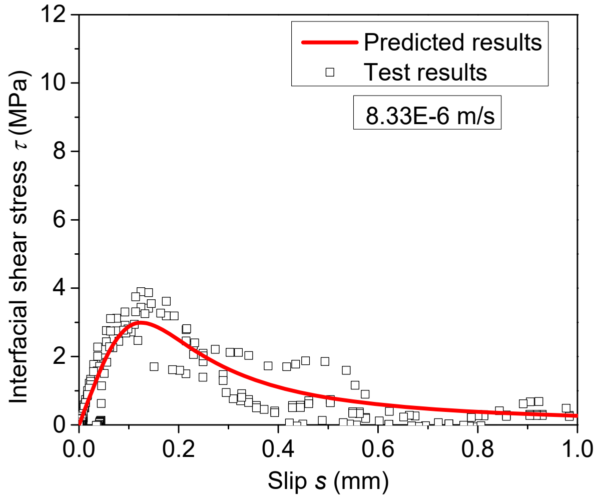

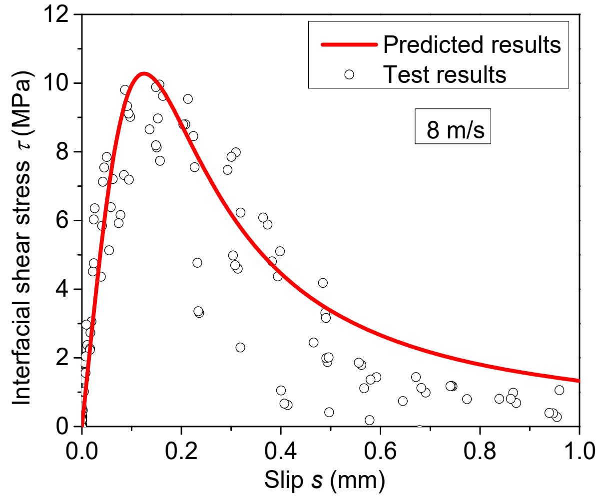

(a) QS1 (5-10 mm) (b) D5 (10-15 mm)

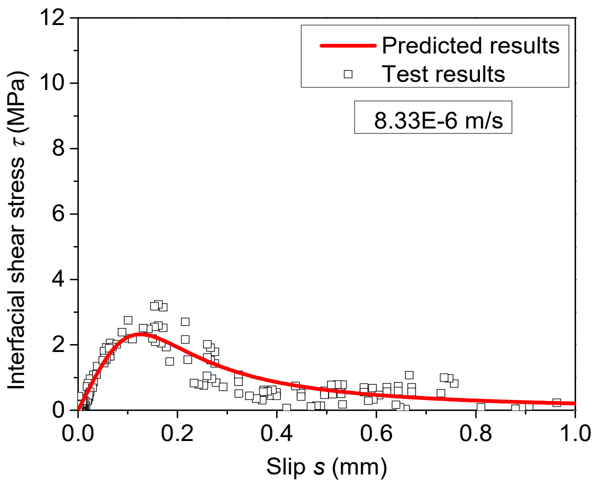

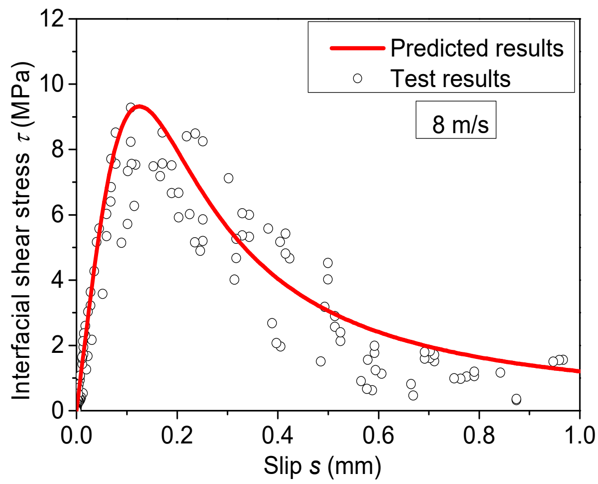

(c) QS2 (10-15 mm) (d) D10 (10-15 mm)

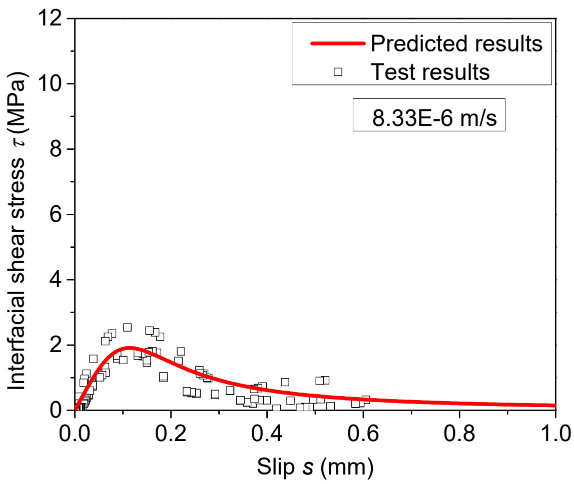

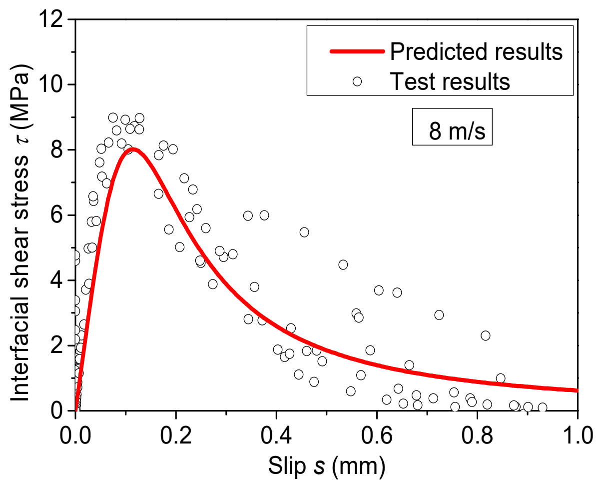

(e) QS3 (15-20 mm) (f) D15 (15-20 mm)

Figure 18. Comparison of predicted and test bond-slip curves

Previous studies have demonstrated that the debonding load, the peak bond stress, and BFRP strain distributions can be obtained by using the proposed bond-slip models in the previous studies [60-62]. The debonding load and strain distribution can be directly obtained from the test data. Therefore, the validation of the proposed bond-slip models can be conducted regarding the debonding load and strain distribution. The debonding load can be obtained by incorporating the interfacial fracture energy under static loadings. The proposed dynamic interfacial fracture energy $G_{f,d}$ can be used to replace the static one to obtain the dynamic results. The formula can be expressed as follows [22, 24, 63]:

$$P_u = b_f \sqrt{2E_f t_f G_f} \tag{10}$$

By substituting the dynamic interfacial fracture energy $G_{f,d}$ into Equation (10), the dynamic debonding load can be obtained accordingly. It is observed that the predicted debonding loads by incorporating the proposed interfacial energy match well with the experimental results. Figure 19 shows the mean value of 0.97 and the corresponding coefficient of variation (COV) of 0.06 between the predicted and experimental results.

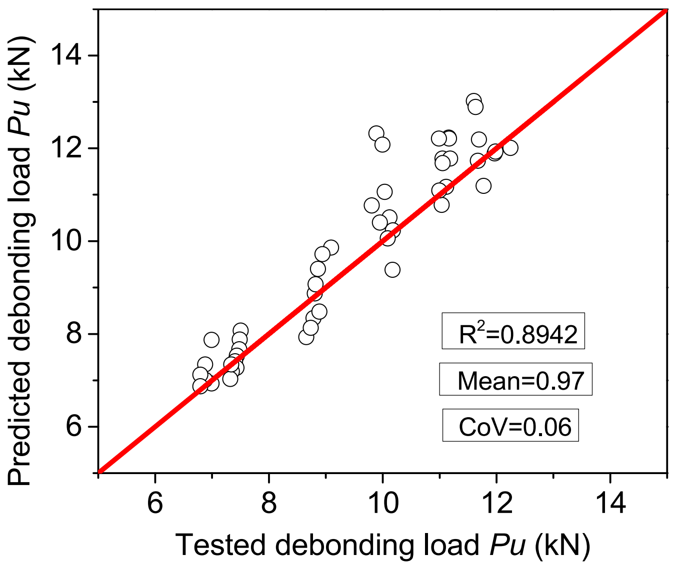

Figure 19. Comparison between the predicted and experimental debonding load

5. Conclusion

The present study experimentally investigated the mechanical properties of the dynamic interfacial bond between BFRP sheets and concrete with different aggregate sizes. Through the single-lap shear tests, the failure mode, bond strength, strain distribution and bond-slip response were obtained and discussed. The following observations and conclusions can be drawn:

(1) Debonding failure mode changed with strain rate; the fracture surface shifted from concrete substrate layer to the concrete-epoxy interface with the increase of strain rate.

(2) The tested specimens under dynamic loadings exhibited more ductile behaviour because of the improved debonding load and the ultimate slip. Compared to the static results, the maximum increments of the ultimate debonding load for Specimens with aggregate sizes of 5-10 mm, 10-15 mm and 15-20mm were 74%, 76%, and 95% at the loading speed of 8 m/s, respectively.

(3) The strain distribution gradient under high dynamic loading was steeper than that under quasi-static loading, indicating the shorter shear stress transfer zone under dynamic loading.

(4) The reduction of peak shear stress was observed for specimens with larger aggregates under the same loading rate. The maximum increments of peak shear stress at the loading speed of 8 m/s for Specimens with aggregates of 5-10mm, 10-15mm and 15-20mm were 77%, 75%, and 74%, respectively, as compared to the static peak shear stress.

(5) Through validating the testing results, a dynamic bond-slip model by incorporating the coarse aggregate size and strain rate was proposed to predict the debonding load and shear stress and slip response of the BFRP-to-concrete interface under dynamic loading.

Acknowledgement

The authors thank the Australian Research Council (ARC LP150100259) for its financial support.

References

[1] T. Ngo, P. Mendis, T. Krauthammer. Behavior of Ultrahigh-Strength Prestressed Concrete Panels Subjected to Blast Loading. J Struct Eng 133 (11) (2007) 1582-90.
[2] X. Zhou, V. Kuznetsov, H. Hao, J. Waschl. Numerical Prediction of Concrete Slab Response to Blast Loading. International Journal of Impact Engineering 35 (10) (2008) 1186-200.
[3] J. Cui, H. Hao, Y. Shi. Discussion on the Suitability of Concrete Constitutive Models for High-Rate Response Predictions of Rc Structures. International Journal of Impact Engineering 106 (2017) 202-16.
[4] Q. Li, H. Meng. About the Dynamic Strength Enhancement of Concrete-Like Materials in a Split Hopkinson Pressure Bar Test. Int J Solids Struct 40 (2) (2003) 343-60.
[5] Y. Hao, H. Hao, G. Jiang, Y. Zhou. Experimental Confirmation of Some Factors Influencing Dynamic Concrete Compressive Strengths in High-Speed Impact Tests. Cement Concrete Res 52 (2013) 63-70.
[6] Y. Hao, H. Hao. Numerical Evaluation of the Influence of Aggregates on Concrete Compressive Strength at High Strain Rate. International journal of protective structures 2 (2) (2011) 177-206.
[7] T. Akçaoğlu, M. Tokyay, T. Çelik. Effect of Coarse Aggregate Size on Interfacial Cracking under Uniaxial Compression. Mater Lett 57 (4) (2002) 828-33.
[8] X. Shi, F. Collins, X. Zhao, Q. Wang. Mechanical Properties and Microstructure Analysis of Fly Ash Geopolymeric Recycled Concrete. Journal of hazardous materials 237 (2012) 20-9.
[9] J. Teng, J.-F. Chen, S.T. Smith, L. Lam. Frp: Strengthened Rc Structures. AIP Conf Proc (2002) 266.
[10] J.G. Teng, J.F. Chen, S.T. Smith, L. Lam. Behaviour and Strength of Frp-Strengthened Rc Structures: A State-of-the-Art Review. Proceedings of the institution of civil engineers-structures and buildings 156 (1) (2003) 51-62.
[11] Y.-F. Wu, C. Jiang. Effect of Load Eccentricity on the Stress–Strain Relationship of Frp-Confined Concrete Columns. Compos Struct 98 (2013) 228-41.
[12] W. Chen, H. Hao, D. Hughes, Y. Shi, J. Cui, Z.-X. Li. Static and Dynamic Mechanical Properties of Expanded Polystyrene. Materials & Design 69 (2015) 170-80.
[13] T.M. Pham, H. Hao. Behavior of Fiber-Reinforced Polymer-Strengthened Reinforced Concrete Beams under Static and Impact Loads. International Journal of Protective Structures 8 (1) (2017) 3-24.
[14] X. Zhang, P. Wang, M. Jiang, H. Fan, J. Zhou, W. Li, L. Dong, H. Chen, F. Jin. Cfrp Strengthening Reinforced Concrete Arches: Strengthening Methods and Experimental Studies. Compos Struct 131 (2015) 852-67.
[15] B. Fu, J.G. Teng, J.F. Chen, G.M. Chen, Y.C. Guo. Concrete Cover Separation in Frp-Plated Rc Beams: Mitigation Using Frp U-Jackets. J Compos Constr 21 (2) (2016) 04016077.
[16] J. Huo, J. Liu, Y. Lu, J. Yang, Y. Xiao. Experimental Study on Dynamic Behavior of Gfrp-to-Concrete Interface. Eng Struct 118 (2016) 371-82.

[17] W. Chen, H. Hao, M. Jong, J. Cui, Y. Shi, L. Chen, T.M. Pham. Quasi-Static and Dynamic Tensile Properties of Basalt Fibre Reinforced Polymer. Compos B Eng 125 (2017) 123-33.
[18] T.M. Pham, H. Hao. Axial Impact Resistance of Frp-Confined Concrete. J Compos Constr 21 (2) (2016) 04016088.
[19] H. Hao, E.K. Tang. Numerical Simulation of a Cable-Stayed Bridge Response to Blast Loads, Part Ii: Damage Prediction and Frp Strengthening. Eng Struct 32 (10) (2010) 3193-205.
[20] P. Buchan, J. Chen. Blast Resistance of Frp Composites and Polymer Strengthened Concrete and Masonry Structures–a State-of-the-Art Review. Compos B Eng 38 (5-6) (2007) 509-22.
[21] D. Zhang, X.-L. Gu, Q.-Q. Yu, H. Huang, B. Wan, C. Jiang. Fully Probabilistic Analysis of Frp-to-Concrete Bonded Joints Considering Model Uncertainty. Compos Struct 185 (2018) 786-806.
[22] B. Wan, C. Jiang, Y.-F. Wu. Effect of Defects in Externally Bonded Frp Reinforced Concrete. Constr Build Mater 172 (2018) 63-76.
[23] Z. Wu, S. Islam, H. Said. A Three-Parameter Bond Strength Model for Frp—Concrete Interface. J Reinf Plast Comp 28 (19) (2009) 2309-23.
[24] Y.-F. Wu, C. Jiang. Quantification of Bond-Slip Relationship for Externally Bonded Frp-to-Concrete Joints. J Compos Constr 17 (5) (2013) 673-86.
[25] Y.-F. Wu, X.-S. Xu, J.-B. Sun, C. Jiang. Analytical Solution for the Bond Strength of Externally Bonded Reinforcement. Compos Struct 94 (11) (2012) 3232-9.
[26] I. Iovinella, A. Prota, C. Mazzotti. Influence of Surface Roughness on the Bond of Frp Laminates to Concrete. Constr Build Mater 40 (2013) 533-42.
[27] D. Shen, Y. Ji, F. Yin, J. Zhang. Dynamic Bond Stress-Slip Relationship between Basalt Frp Sheet and Concrete under Initial Static Loading. J Compos Constr 19 (6) (2015) 04015012.
[28] J. Huo, J. Liu, X. Dai, J. Yang, Y. Lu, Y. Xiao, G. Monti. Experimental Study on Dynamic Behavior of Cfrp-to-Concrete Interface. J Compos Constr 20 (5) (2016) 04016026.
[29] J.W. Shi, H. Zhu, Z.S. Wu, G. Wu. Experimental Study of the Strain Rate Effect of Frp Sheet-Concrete Interface. China Civil Eng J 45 (12) (2012) 99-107.
[30] D. Shen, H. Shi, Y. Ji, F. Yin. Strain Rate Effect on Effective Bond Length of Basalt Frp Sheet Bonded to Concrete. Constr Build Mater 82 (2015) 206-18.
[31] J. Pan, C.K. Leung. Effect of Concrete Composition on Frp/Concrete Bond Capacity. J Compos Constr 11 (6) (2007) 611-8.
[32] C. Yuan, W. Chen, T.M. Pham, H. Hao. Effect of Aggregate Size on Bond Behaviour between Basalt Fibre Reinforced Polymer Sheets and Concrete. Compos B Eng 158 (2019) 459-74.
[33] J. Pan, C.K. Leung. Effect of Concrete Composition on Interfacial Parameters Governing Frp Debonding from the Concrete Substrate. Adv Struct Eng 12 (5) (2009) 627-37.
[34] C. Yuan, W. Chen, T.M. Pham, H. Hao. Bond Behaviour between Hybrid Fiber Reinforced Polymer Sheets and Concrete. Constr Build Mater 210 (2019) 93-110.
[35] C. Yuan, W. Chen, T.M. Pham, H. Hao. Bond Behavior between Basalt Fibres Reinforced Polymer Sheets and Steel Fibres Reinforced Concrete. Eng Struct 176 (2018) 812-24.
[36] M.S. Salimian, D. Mostofinejad. Experimental Evaluation of Cfrp-Concrete Bond Behavior under High Loading Rates Using Particle Image Velocimetry Method. J Compos Constr 23 (3) (2019) 04019010.
[37] M.B. Ouezdou, A. Belarbi, S.-W. Bae. Effective Bond Length of Frp Sheets Externally Bonded to Concrete. Int J Concr Struct M 3 (2) (2009) 127-31.
[38] B. Ghiassi, J. Xavier, D.V. Oliveira, P.B. Lourenço. Application of Digital Image Correlation in Investigating the Bond between Frp and Masonry. Compos Struct 106 (2013) 340-9.

[39] X. Xiao. Dynamic Tensile Testing of Plastic Materials. Polymer Testing 27 (2) (2008) 164-78.
[40] H.C. Biscaia, C. Chastre, I.S. Borba, C. Silva, D. Cruz. Experimental Evaluation of Bonding between Cfrp Laminates and Different Structural Materials. J Compos Constr 20 (3) (2015) 04015070.
[41] J.G. Dai, T. Ueda, Y. Sato. Development of the Nonlinear Bond Stress–Slip Model of Fiber Reinforced Plastics Sheet–Concrete Interfaces with a Simple Method. J Compos Constr 9 (1) (2005) 52-62.
[42] K. Liu, Y.-F. Wu. Analytical Identification of Bond–Slip Relationship of Eb-Frp Joints. Compos B Eng 43 (4) (2012) 1955-63.
[43] C. Jiang, B. Wan, J. Omboko. Enhancing Frp-to-Concrete Bond Behavior by Epoxy Ribs. Special Publication 327 (2018) 25.1-.14.
[44] C. Jiang, Y.-F. Wu, J.-F. Jiang. Effect of Aggregate Size on Stress-Strain Behavior of Concrete Confined by Fiber Composites. Compos Struct 168 (2017) 851-62.
[45] Z.P. Bažant, Q. Yu. Universal Size Effect Law and Effect of Crack Depth on Quasi-Brittle Structure Strength. J Eng Mech 135 (2) (2009) 78-84.
[46] H.-T. Wang, G. Wu. Bond-Slip Models for Cfrp Plates Externally Bonded to Steel Substrates. Compos Struct 184 (2018) 1204-14.
[47] H. Toutanji, P. Saxena, L. Zhao, T. Ooi. Prediction of Interfacial Bond Failure of Frp–Concrete Surface. J Compos Constr 11 (4) (2007) 427-36.
[48] Y. Yun, Y.-F. Wu, W.C. Tang. Performance of Frp Bonding Systems under Fatigue Loading. Eng Struct 30 (11) (2008) 3129-40.
[49] Y. Yun, Y.-F. Wu. Durability of Cfrp–Concrete Joints under Freeze–Thaw Cycling. Cold Regions Science and Technology 65 (3) (2011) 401-12.
[50] X.Z. Lu, J.G. Teng, L.P. Ye, J.J. Jiang. Bond–Slip Models for Frp Sheets/Plates Bonded to Concrete. Eng Struct 27 (6) (2005) 920-37.
[51] S. Popovics. A Numerical Approach to the Complete Stress-Strain Curve of Concrete. Cement Concrete Res 3 (5) (1973) 583-99.
[52] Y. Sato, F.J. Vecchio. Tension Stiffening and Crack Formation in Reinforced Concrete Members with Fiber-Reinforced Polymer Sheets. J Struct Eng 129 (6) (2003) 717-24.
[53] K. Nakaba, T. Kanakubo, T. Furuta, H. Yoshizawa. Bond Behavior between Fiber-Reinforced Polymer Laminates and Concrete. Structural Journal 98 (3) (2001) 359-67.
[54] W. Sun, X. Peng, Y. Yu. Development of a Simplified Bond Model Used for Simulating Frp Strips Bonded to Concrete. Compos Struct 171 (2017) 462-72.
[55] H.B. Pham, R. Al-Mahaidi. Modelling of Cfrp-Concrete Shear-Lap Tests. Constr Build Mater 21 (4) (2007) 727-35.
[56] K.V. Subramaniam, C. Carloni, L. Nobile. Width Effect in the Interface Fracture During Shear Debonding of Frp Sheets from Concrete. Eng Struct 74 (4) (2007) 578-94.
[57] L. Bizindavyi, K. Neale. Transfer Lengths and Bond Strengths for Composites Bonded to Concrete. J Compos Constr 3 (4) (1999) 153-60.
[58] C. Carloni, K.V. Subramaniam. Investigation of Sub-Critical Fatigue Crack Growth in Frp/Concrete Cohesive Interface Using Digital Image Analysis. Compos B Eng 51 (2013) 35-43.
[59] C. Pellegrino, D. Tinazzi, C. Modena. Experimental Study on Bond Behavior between Concrete and Frp Reinforcement. J Compos Constr 12 (2) (2008) 180-9.
[60] Y.-W. Zhou, Y.-F. Wu, Y. Yun. Analytical Modeling of the Bond–Slip Relationship at Frp-Concrete Interfaces for Adhesively-Bonded Joints. Compos B Eng 41 (6) (2010) 423-33.
[61] J.G. Dai, T. Ueda, Y. Sato. Bonding Characteristics of Fiber-Reinforced Polymer Sheet-Concrete Interfaces under Dowel Load. J Compos Constr 11 (2) (2007) 138-48.

[62] W. Sun, X. Peng, H.F. Liu, H.P. Qi. Numerical Studies on the Entire Debonding Propagation Process of Frp Strips Externally Bonded to the Concrete Substrate. Constr Build Mater 149 (2017) 218-35.
[63] J. Dai, T. Ueda, Y. Sato. Bonding Characteristics of Fiber-Reinforced Polymer Sheet-Concrete Interfaces under Dowel Load. J Compos Constr 11 (2) (2007) 138-48.